Mechanistic model to predict frequency and amplitude of Density Wave Oscillations in vertical upflow boiling

Lucas E. O'Neill, Issam Mudawar *

Purdue University Boiling and Two-Phase Flow Laboratory (PU-BTPFL), School of Mechanical Engineering, Purdue University, 585 Purdue Mall, West Lafayette, IN 47907, USA

A R T I C L E   I N F O

A B S T R A C T

Modeling of two-phase flow transient behavior and instabilities has traditionally been one of the more challenging endeavors in heat transfer research due to the need to distinguish between a wide range of instability modes systems can manifest depending on differences in operating conditions, as well as the difficulty in experimentally determining key characteristics of these phenomena. This study presents a new mechanistic model for Density Wave Oscillations (DWOs) in vertical upflow boiling using conclusions drawn from analysis of flow visualization images and transient experimental results as a basis from which to begin modeling. Counter to many prior studies attributing DWOs to feedback effects between flow rate, pressure drop, and flow enthalpy causing oscillations in position of the bulk boiling boundary, the present instability mode stems primarily from body force acting on liquid and vapor phases in a separated flow regime leading to liquid accumulation in the near-inlet region of the test section, which eventually departs and moves along the channel, acting to re-wet liquid film along the channel walls and re-establish annular, co-current flow. This process was modeled by dividing the test section into three distinct control volumes and solving transient conservation equations for each, yielding predictions of frequencies at which this process occurs as well as amplitude of associated pressure oscillations. Values for these parameters were validated against an experimental database of 236 FC-72 points and show the model provides good predictive accuracy and capably captures the influence of parametric changes to operating conditions.

© 2018 Elsevier Ltd. All rights reserved.

1. Introduction

1.1. Importance of flow boiling dynamic behavior in space-based applications

To meet increasingly stringent thermal design constraints posed by dual trends of miniaturization and increased performance across multiple industries, thermal design engineers are considering two-phase flow thermal management systems which capitalize on both sensible and latent heat to offer orders of magnitude improvements in heat transfer performance [1]. Researchers at the Purdue University Boiling and Two-Phase Flow Laboratory (PU-BTPFL) and other organizations have investigated many different configurations to best utilize phase change heat transfer for varying applications, including capillary-driven devices [2–4], pool boiling thermosyphons [5–7], falling film [8,9], channel flow boiling [10,11], micro-channel boiling [12–16], jet impingement [17–20], and spray [21–27], as well as hybrid configurations [28–31] involving two or more of these schemes.

Thermal management systems utilizing phase change heat transfer are particularly attractive options for utilization in aerospace thermal-fluid systems where their high heat transfer coefficients allow significant reductions in size and weight of hardware, both critical design parameters in aerospace applications. This has led space agencies worldwide to fund further development of the technology to allow implementation in both space vehicles and planetary bases. Current targets for adoption of phase change technologies include Thermal Control Systems (TCSs), which control temperature and humidity of the operating environment, heat receiver and heat rejection systems for power generating units, and Fission Power Systems (FPSs), which are projected to provide high power as well as low mass to power ratio [32–34].

Limiting the adoption rate of phase-change heat transfer for these technologies is the presence of complex phenomena related to buoyancy and surface tension present in multiphase flows which can affect critical aspects such as flow regime, phase distribution, and even the nucleation process itself. Many design tools for phase change thermal management rely on empirically

Nomenclature

A	amplitude, area
D_H	hydraulic diameter
F	force
f	frequency, friction factor
G	mass velocity
g_e	gravitational constant
H	height of flow channel's cross-section; digital filter transfer function
h_{fg}	latent heat of vaporization
L	length
l	length
L_d	development length of flow channel
L_e	exit length of flow channel
L_h	heated length of flow channel
M	momentum
m	mass
$\dot{m}$	mass flow rate
MAE	mean absolute error
N	number of data points
N_{pch}	phase change number
N_{sub}	subcooling number
P	pressure
p	perimeter
P_{in}	pressure at inlet to heated portion of channel
ΔP	pressure drop
Q	total heat input to channel
q''	heat flux on heated perimeter of channel
r	radius
Re	Reynolds number
t	time
u	velocity
v	specific volume
W	width of flow channel's cross-section
x	quality
x_e	thermodynamic equilibrium quality
x_f	flow quality
z	stream-wise position; digital domain variable

Greek symbols

α	void fraction
Γ	mass transfer rate
μ	dynamic viscosity
ρ	density
τ	shear stress
θ	percentage of predictions within 30% of experimental value
ζ	percentage of predictions within 50% of experimental value

Subscripts

12	evaluated between regions 1 and 2
23	evaluated between regions 2 and 3
A	accelerational
a	adiabatic
ave	average
c	cross-section; core
d	diabatic (heated)
DWO	property of Density Wave Oscillation (such as amplitude or frequency)
exp	experimental (measured)
F	friction
f	saturated liquid
FBM	flow boiling module
G	gravitational
g	saturated vapor
HDF	property of HDF
in	inlet to channel
$interface$	evaluated at the interface (such as shear stress or perimeter)
k	phase indictor
m	heated wall identifier (a for heater H_a or b for heater H_b)
PC	phase change
$pred$	predicted
SE	single event
tot	total (indicates parameter is evaluated over the total length of Region 3)
w	wetted
$wall$	evaluated for the channel wall (such as shear stress or perimeter)
z	stream-wise position
$Zivi$	evaluated using Zivi void fraction correlation
2φ	two-phase

Superscripts

0	value at initial time (equal to Region 1 value for all Region 3 parameters)
n	indicates current time step

Abbreviations

CHF	Critical Heat Flux
DWO	Density Wave Oscillation
FBM	Flow Boiling Module
HDF	High Density Front
LDV	Laser Doppler Velocimetry
PCI	Parallel Channel Instability
PDO	Pressure Drop Oscillation

correlated expressions for key parameters that were developed based on testing in a certain orientation in Earth's gravity. From the hyper-gravity associated with launch, to the micro-gravity of orbit and/or deep space, to the varying gravitational fields associated with operation on various extra-terrestrial bodies, any system designed for aerospace applications will need to be robust to drastic changes in operating conditions which fall outside the intended range of existing empiric and semi-empiric design tools. Prior studies conducted with the aid of parabolic flight have shown changes in local acceleration lead to dynamic changes in flow boiling behavior, with similar operating conditions tested in micro-gravity and hyper-gravity environments yielding significant difference in flow boiling heat transfer [35,36]. It is likely more sophisticated design tools, such as mechanistic models and

computational schemes, could better predict this behavior as they are based less on prior experimental results, which may or may not apply, and more on the dominant underlying physical processes.

In addition to changes in system performance due to varying local acceleration across a mission's lifecycle, continuous changes to ambient thermal environment of the system often necessitate changes in operation mode. Whether due to cyclical solar exposure in orbiting vehicles, differences in ambient temperature between operations in space (transit) and some terrestrial environment (Moon, Mars, *etc.*), or changes in thermal loading associated with periodic operation of high-energy instruments, it is likely any dedicated space-based two-phase flow thermal management system will need to operate across a range of flow rates, heat fluxes, and pressures. Many studies have shown how changes to these param-

eters can instigate the onset of flow boiling instabilities, expressing transition criteria in the form of both stability maps [37–39] and transition correlations [40–43], but further study of the characteristics of these instabilities and other transient phenomena is necessary.

1.2. Flow boiling instabilities and transient phenomena

The origin of the study of two-phase flow instabilities is commonly attributed to Ledinegg [44], who discovered for certain operating conditions two-phase flow systems experience a jump from an unstable location to a stable location on the system's internal-external pressure curve. This manifests as a change in both system mass velocity and operating pressures.

Throughout the latter half of the 20th century, researchers investigated less noticeable, more persistent transient phenomena found in two-phase flow systems [45–47], with special attention paid to Density Wave Oscillations (DWOs) [48,49]. It was around this time that Boure et al. published their seminal review of two-phase flow instabilities [50], which both summarized state-of-the-art understanding of two-phase flow transient phenomena and instabilities at the time and paved the way for future investigations in the field.

Present day researchers continue characterizing instabilities and transient behavior observed in experimental two-phase flow systems, focusing on DWOs [51–55], Parallel Channel Instability (PCI) [56–58], Pressure Drop Oscillations (PDOs) [59–61], and interaction of multiple instability modes [62,63]. Recent reviews, such as those by Tadrist [64], Kakac and Bon [65], and Ruspini et al. [66] provide updated surveys of literature relating to phenomena first reported by Boure et al. [50].

Recent experimental studies concerning other facets of two-phase flows (such as heat transfer, pressure drop, *etc.*) have also begun to focus more on aspects of transient system behavior, centering on bubble dynamics in micro-channels [67], temperature, pressure, and heat transfer fluctuations unassociated with instabilities [68–72], transient flow pattern transitions [73], and even system response to manually induced periodicity [74]. Much of the transient behavior observed in these studies can likely be related to either instabilities present in two-phase flow systems or externally induced oscillations, and use of a systematic analysis approach by the two-phase flow community could greatly homogenize interpretation of results.

Of the many aspects of transient two-phase flow currently being studied, however, only DWOs are of particular interest to the present study, and, as such, a more detailed review of key works in the field will be provided.

1.3. Density Wave Oscillations

Although the first experimental observation of DWOs is commonly attributed to Serov [48], it wasn't until nearly two decades later that researchers began devoting significant time to better understanding and categorizing these oscillations. It is commonly held that their occurrence is due to feedback effects between vapor generation rate, flow rate, and system pressure drop, which cause the Onset of Significant Vapor (OSV, also sometimes referred to as the onset of bulk boiling) point within the boiling channel to oscillate, thereby altering channel pressure drop characteristics and causing flow rate to fluctuate, and this is the point from which analytic works sought to begin modeling.

Ishii provided one of the first comprehensive experimental and analytic assessments of the phenomenon [75]. The phenomenon was modeled using classic stability analysis whereby governing equations were transformed into the *s*-domain (frequency domain) and expressed in terms of transfer function between different

parameters. This allowed system stability at a given operating point to be assessed using graphical 'stability test criterion' (such as that presented by Nyquist [76]). Stability boundaries for full ranges of operating conditions were determined by employing the D-Partition Method, which divides the multi-dimensional parameter space into regions bounded by harmonic frequency surfaces and singular surfaces, with stability of each surface found by testing a single point within each using the aforementioned graphical stability test criterion.

Ishii utilized experimental results from several studies [77–79], demonstrating his method for determining overall system stability by reducing the multi-dimensional parameter space to 2-dimensional for presentation, using subcooling and phase-change numbers as *x*- and *y*-coordinates, respectively. These parameters were defined as

$$N_{sub} = \frac{h_f - h_{in}}{h_{fg}} \frac{v_g - v_f}{v_f} \tag{1}$$

and

$$N_{pch} = \frac{Q}{\dot{m} h_{fg}} \frac{v_g - v_f}{v_f}, \tag{2}$$

and are still commonly utilized in literature presenting stability maps for flow boiling.

Following shortly after Ishii, Yadigaroglu and Bergles [49] performed both analytic and experimental investigations into DWOs occurring in flow boiling of Freon-113. Their analytic work followed similar lines of analysis as that of Ishii [75], and their experimental work revealed periods of oscillation in the range of 2–10 s.

Fukuda and Kobori [80] also investigated DWOs using both experimental and analytic methods, employing a test section composed of two parallel channels. They distinguished two separate types of DWOs from experimental observations: Type I, occurring at near-zero steam exit quality and largely influenced by gravitational pressure drop, and Type II, occurring at high steam exit quality and largely influenced by frictional pressure drop. This classification of DWOs into different types based on key driving behavior is particularly relevant for the analysis to be presented in the present study.

Around the same time, Belblidia and Bratianu [81] presented a review of existing literature concerning DWOs. They also noted the possibility of different driving forces leading to the manifestation of the instability, and provided detailed analysis of the different modeling approaches used (mixture models, two-fluid models, *etc.*) and their effect on predictions of stability. Further, they made the key observation that existing literature was far more concerned with prediction of boundaries for stable system observation, and characterization of unstable behavior was of little importance.

Achard et al. [82] built on previous analytic works concerning DWOs by utilizing Hopf-Bifurcation analysis in an attempt to characterize frequency and amplitude of oscillations. Their analysis indicated that the concept of a 'stability-boundary' was an oversimplification, and that for operating conditions in a region sufficiently close to calculated stability bounds the system would likely exhibit limit-cycle oscillations.

Although largely building on aforementioned analysis approaches, Lahey and Podowski [47] provided a very comprehensive, detailed analytic treatment of DWOs and other instability modes within multi-phase flow systems. Their analytic work primarily utilizes a drift flux modeling approach to the system(s) in question.

In the early 1990s two experimental studies by Yuncu [62] and Wang et al. [83], respectively, served to significantly advance the understanding of mechanisms behind and manifestation of DWOs. Yuncu investigated flow boiling of Freon 11 and observed both

DWOs and PDOs, with DWOs occurring at higher frequencies than PDOs within his experimental system. Period of DWOs was found to be 1–1.5 s, and amplitude of DWOs was found to increase with increases in both mass flux and heat flux. Wang et al. investigated flow boiling of water in a single channel. Instead of the classic stability-theory approach to modeling onset of instability used in many prior works, they chose to correlate their experimental data to develop expressions for 'limiting heat flux' and 'limiting quality' for onset of DWOs. They also observed DWO periods on the order of 1.5 s.

More recently, Schlichting et al. [63] presented detailed numeric analysis on stability boundaries and behavior of interacting DWO and PDO instability modes for a proposed NASA testbed using FC-72 as the working fluid. Building on prior stability analysis work of Lahey and Podowski [47], they employed Hopf-bifurcation analysis and characterized limit cycle oscillations expected to be present within the system.

This classic stability analysis approach was taken even further by Pandey and Singh [84], who modeled the interaction between Ledinegg instability and DWOs as phenomena giving rise to Bogdanov-Takens bifurcation. Their work was purely analytic, and constitutes one of the most comprehensive uses of classic stability theory available in contemporary literature.

Despite significant advances in both experimental and analytic investigations into DWOs, many questions remain surrounding their formation and characteristic behavior. In particular, the idea proposed by Fukuda and Kobori [80] (among others) that DWOs can form as a result of different dominant forces based on operating conditions has relevance to the current work, as the test section and operating conditions explored here are atypical for DWO investigation. Almost all prior studies based their analysis on flow boiling through long channels with highly subcooled inlet conditions and finite quality outlet. The present heated length, however, is significantly shorter than that explored in many prior works, and only exhibits typical DWO behavior for cases with finite inlet quality [54]. Due to this, modeling work will follow a novel approach, based on experimentally observed, dominant physical mechanisms.

1.4. Objectives of study

This work is part of an ongoing collaboration between Purdue University Boiling and Two-Phase Flow Laboratory (PU-BTPFL) and NASA Glenn Research Center (GRC) whose ultimate goal is development of the Flow Boiling and Condensation Experiment (FBCE) for the International Space Station (ISS). A summary of scientific developments from the project thus far, including key objectives, experimental methodology, analytic approaches, and other relevant works, can be found in a recent summary article [85].

The current study deals with flow boiling and augments prior work dealing with experimental investigation and prediction of key design parameters including heat transfer coefficient [86–89], pressure drop [53,90–91], and critical heat flux [92–98], with development of a mechanistic model for prediction of frequency and amplitude of DWO induced pressure oscillations evident in vertical upflow boiling with finite inlet quality. Objectives for the study are as follows:

(1) Use transient pressure signals and flow visualization images to provide a comprehensive characterization of DWOs along with a physically consistent explanation for their manifestation in vertical upflow boiling.
(2) Use key findings from experimental results as a basis from which to begin mechanistic modeling of the DWO phenomenon as observed in the present dataset, with the goal

of creating a model capable of providing valid predictions for frequency and amplitude of DWO induced oscillations for a wide range of operating conditions.
(3) Evaluate model performance using experimental results to determine strengths and weaknesses of the modeling approach, identifying key goals for future analysis work.

This work builds directly on prior studies by the current authors [53,54], which detected and investigated the DWO phenomenon using transient pressure measurements throughout the system. It should also be noted that the present work is the companion study to another [55] presenting extensive analysis of the DWO phenomenon as it manifests in vertical upflow boiling with finite inlet quality using flow visualization images and experimentally determined values of frequency and amplitude of oscillation. Experimental outcomes from these studies help inform the modeling work undertaken here.

2. Experimental methods

The present work is primarily analytic in nature, but relies upon experimental results from two separate sets of experiments for validation of the model developed herein. For this reason, a brief overview of experimental methods will be provided. For more detailed information concerning experimental methods, the reader is advised to consult [53,54] for Year 1 and Year 2 datasets, respectively.

2.1. Experimental facilities

The test module used in both sets of experiments is the Flow Boiling Module (FBM), shown schematically in Fig. 1(a) and photographed in Fig. 1(b). Developed as a part of the FBCE and designed towards eventual use on the ISS, the FBM is instrumented to allow high-speed photography through transparent polycarbonate sidewalls while simultaneously providing detailed flow boiling heat transfer and pressure drop measurements made over the heated length. Constructed by clamping three pieces of transparent polycarbonate plastic (Lexan) between two aluminum support plates, Fig. 1(a) shows the middle polycarbonate plate is milled out to create a rectangular 2.5-mm by 5-mm flow channel with a development length of 327.9 mm followed by a heated length of 114.6 mm and concluding with a 60.9-mm exit length.

The heated length is created by recessing oxygen-free copper slabs flush with two opposite walls of the channel. Each copper slab has six 4.5-mm wide, 16.4-mm long, 188-Ω resistive heaters soldered to their backs, evenly spaced with small gaps between successive heaters to allow temperature measurements made using type-E thermocouples. Heat flux to each wall can be controlled separately, although the present study deals only with cases where heat is supplied evenly to both heated walls.

Fig. 1(b) presents photos of the actual FBM with key points identified. Temperature measurement locations shown include both inlet and outlet fluid temperature measurements (made using type-E thermocouples inserted in the flow) as well as wall thermocouples for both heated walls. The top view shows the five pressure measurement points, comprised of three along the development length, one upstream of the heated length, and one downstream of the heated length.

Fig. 1(c) and (d) illustrates the flow loops used to gather data in Year 1 and Year 2, respectively. In both cases, an Ismatech MCP-z magnetically-coupled gear pump was used to circulate the working fluid, FC-72, through the system. Exiting the pump, the fluid passed through a filter to remove any particulates before entering a turbine flow meter for flow rate measurement. Downstream of
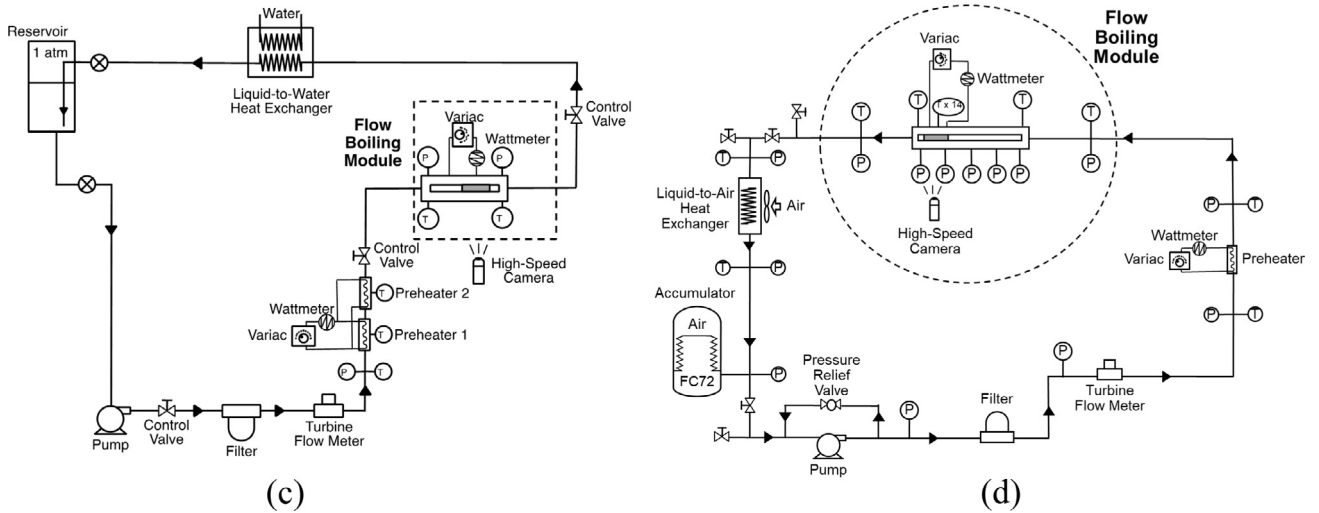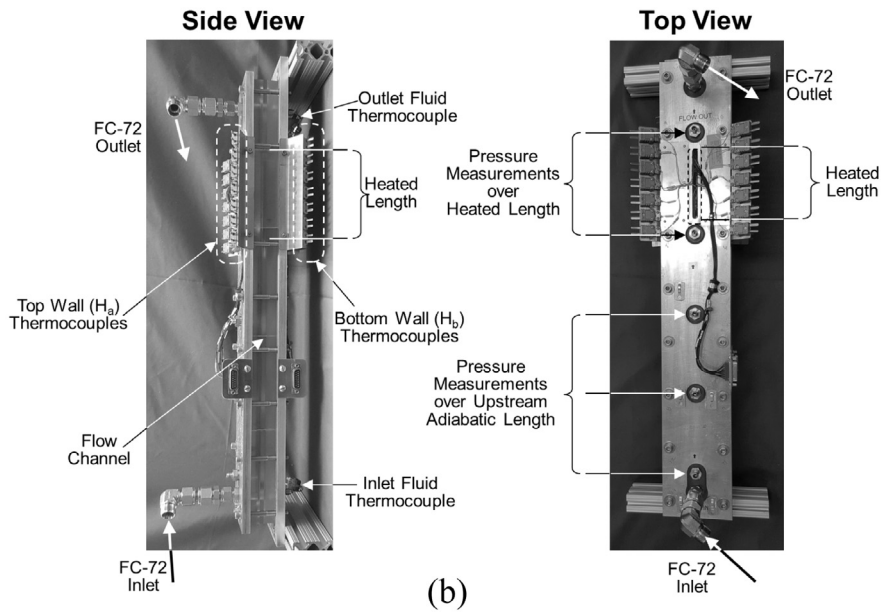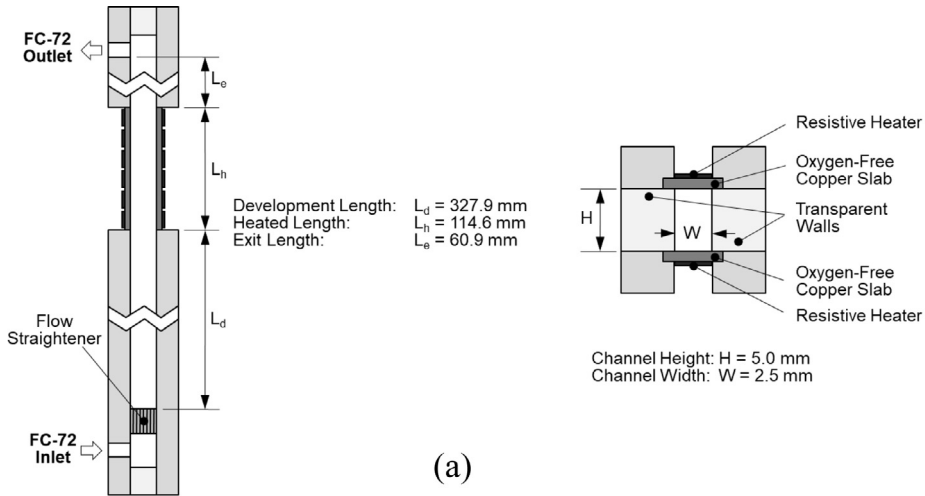
Development Length: L_d = 327.9 mm
Heated Length: L_h = 114.6 mm
Exit Length: L_e = 60.9 mm

Channel Height: H = 5.0 mm
Channel Width: W = 2.5 mm

(a)

(b)

(c)

(d)

Fig. 1. (a) Schematics and (b) photos of Flow Boiling Module (FBM), and schematics of (c) year 1 (2015) and (d) year 2 (2016) experimental flow boiling facilities.

the flow meter, the fluid entered the bulk heater(s) where power was supplied to achieve desired thermodynamic conditions at the inlet to FBM.

In both sets of experiments, wall heat flux in FBM was controlled using the FBM heater control module, which also ensured the module's safety by automatically disabling the power supply

should any of the heated wall temperatures exceed 125 °C (occurring only during the CHF transient for experiments using FC-72 as working fluid). After exiting the test section, the fluid passed through a condenser to return to a subcooled, single-phase liquid state before returning to the pump.

Data throughout both systems were obtained with an NI SCXI-1000 data acquisition system controlled by a LabVIEW code. Pressure transducers were sampled at 200 Hz, allowing high fidelity transient analysis of pressure signals.

Images were captured at a rate of 2000 frames per second (fps) with a pixel resolution of 2040 × 174 spanning the total 114.6-mm heated (diabatic) length. Illumination was provided from the opposite side of the flow channel by blue LEDs, with light passing through a light shaping diffuser (LSD) to enhance illumination uniformity.

A more comprehensive discussion on differences between flow loops used in each respective year can be found in the companion work to the present study [55], which showed that DWO induced pressure oscillations in the test section exhibited repeatability across the two years.

2.2. Operating conditions and measurement uncertainty

Full operating conditions for each set of experiments conducted and details regarding operating procedure can be found in the original experimental studies associated with each [53,54]. The subset of operating conditions used for the current work are provided in Table 1, and correspond to the range of operating conditions for which DWOs were observed in vertical upflow orientation. As mentioned previously, DWOs were not observed in the current test section for operating conditions corresponding to subcooled inlet conditions [54], and dominant hydrodynamic behavior relating to their occurrence departs from classic descriptions of the phenomenon [55]. This will be discussed in more detail in subsequent sections.

Type-E thermocouples with an accuracy of ±0.5 °C were used to measure fluid and heated wall temperatures throughout the facility. Pressure measurements throughout the flow loop were made using pressure transducers with an accuracy of ±0.1%, which corresponds to an accuracy for all pressure drop measurements of ±0.2%. Pressure transducers used in the present study possess a mechanical response time of less than 1 ms, allowing the signal to be sampled at 200 Hz (once every 0.005 s). The turbine flow meter has an accuracy of ±0.1%. The wall heat input was measured with an accuracy of ±0.5 W.

3. Experimental depiction of Density Wave Oscillation (DWO) phenomenon

Prior to undertaking modeling work to predict the amplitude and frequency at which DWOs occur, it is necessary to first provide a description of the phenomenon as observed during experiments. More detailed analysis can be found in prior works by the present authors [53–55], with [55] in particular providing an extensive discussion on mechanisms behind occurrence of DWOs and their characteristics when manifest. For the current study, a brief overview will be provided.

3.1. Flow visualization results

Fig. 2 provides flow visualization image sequences corresponding to flow with mass velocity G = 405.9 kg/m^2 s, inlet quality $x_{e,in}$ = 0.03, FBM heated length inlet pressure P_{in} = 116.4 kPa, and heat flux q'' = 11.0 W/cm^2. Each image encompasses the entire 114.6-mm heated (diabatic) length of FBM, with individual images separated by 0.01 s, giving a total imaging duration of 1 s subdivided evenly into five sections, Fig. 2(a)–(e).

Beginning with Fig. 2(a), flow is clearly seen to be annular throughout the channel length, with a wavy liquid film along the walls and a vapor core in the center of the channel. At this low flow quality some regions of liquid film bridging are apparent, indicating the flow is transitional between slug and annular flow regimes.

As time progresses and analysis shifts to Fig. 2(b), the amount of liquid content in the downstream region is clearly reduced, and an increasing amount of vapor is visible with barely any liquid film. By the middle of Fig. 2(b), it is clear only the upstream portion of the heated length has an appreciable amount of liquid present and the majority of the channel is exposed to vapor. At the very end of Fig. 2(b), however, a liquid wetting front is seen to enter the heated length of the channel, indicated by white arrows.

The beginning images of Fig. 2(c) show the liquid front traversing the entire channel. In the upstream portion, nucleate boiling is clearly visible, while in the downstream region increased vapor content appears to initiate a transition back towards annular flow. Towards the end of Fig. 2(c), flow at the inlet to the heated length transitions away from single-phase liquid and back to annular flow, again indicated with white arrows.

This leads the entire flow-field to revert to a nominal state of annular flow throughout, and as time progresses through Fig. 2 (d) into Fig. 2(e) liquid content is significantly reduced, with vapor occupying the majority of the channel by the middle of Fig. 2(e). Similar to that seen in Fig. 2(b) and (c), this dryout is again followed by the passage of a liquid front through the heated length in Fig. 2(e), again re-wetting the walls, and eventually giving way to annular flow after passing out of the test section.

After observing this cyclical process of annular flow giving way to significantly reduced liquid content (dryout), followed shortly by the passage of a liquid front (High Density Front, HDF), defined as the region composed primarily of liquid denoted by white arrows indicating its front in Fig. 2(b) and back in Fig. 2(c) as well as the same in Fig. 2(e)) through the heated length re-establishing annular flow, it was hypothesized this is the process leading to pressure oscillations observed when analyzing transient experimental measurements.

3.2. Transient pressure results

Fig. 3 provides transient pressure results for the same operating conditions depicted in Fig. 2 illustrating how the cyclical passage of HDFs manifests as pressure oscillations.

Fig. 3(a) shows 20-s duration measurements of pressure at both the inlet and outlet of FBM heated length, with each pressure transducer being sampled at 200 Hz as mentioned in Section 2. These measurements correspond to nominal system steady state, meaning that any oscillations are about a near-constant mean

Table 1
Operating conditions used in present study.

Experiment subset	G [kg/m^2 s]	$x_{e,in}$	q'' [W/cm^2]	P_{in} [kPa]	Number of data points
Year 1 (2015)	190.7–1978.9	0.00–0.69	1.0–22.5	109.7–190.3	192
Year 2 (2016)	199.5–808.8	0.00–0.18	0.0–28.3	130.7–229.3	44
Overall	190.7–1978.9	0.00–0.69	0.0–28.3	109.7–229.3	236
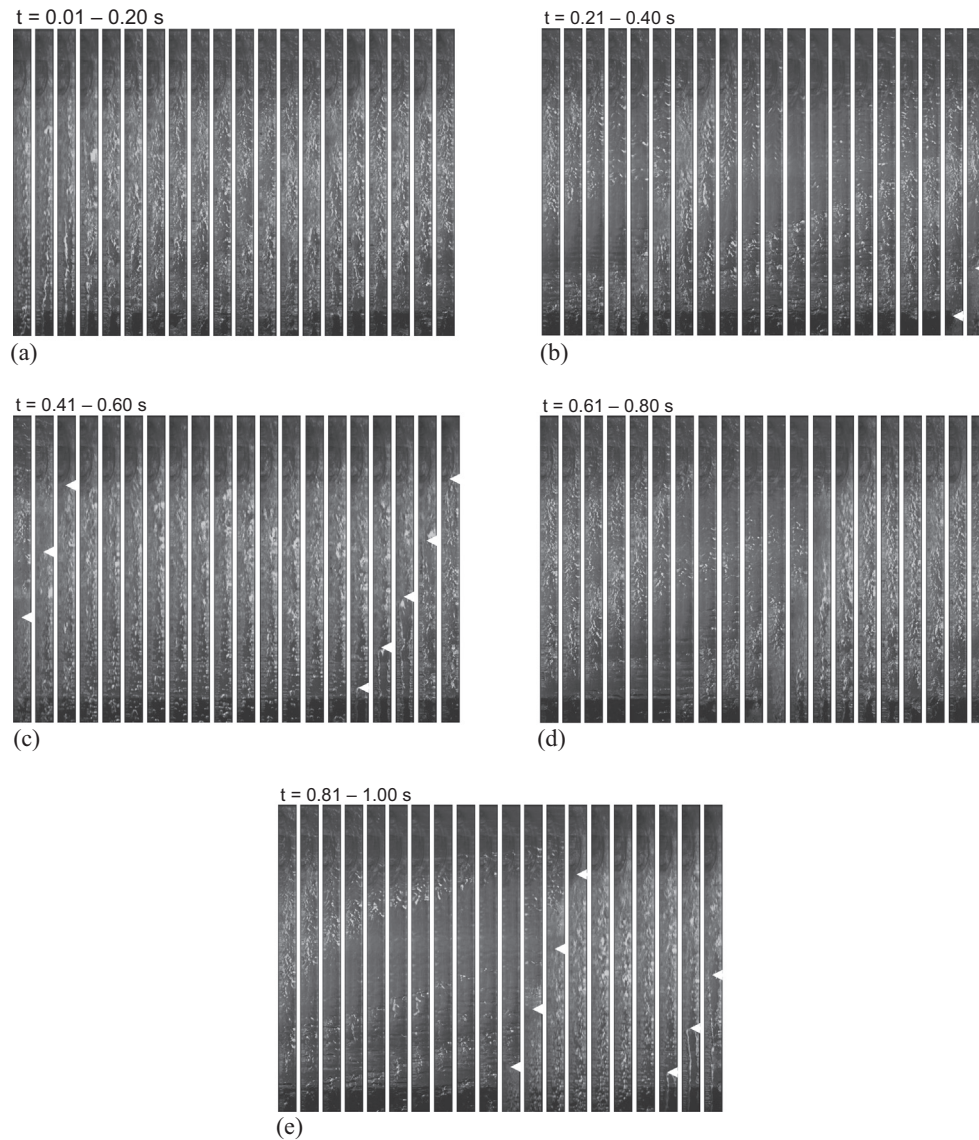
Fig. 2. Consecutive flow visualization image sequences for vertical upflow boiling with G = 405.9 kg/m^{2}s, $x_{e,in}$ = 0.03, P_{in} = 116.4 kPa, and q'' = 11.0 W/cm^2, spanning (a) 0.01–0.20 s, (b) 0.21–0.40 s, (c) 0.41–0.60 s, (d) 0.61–0.80 s, and (e) 0.81–1.00 s. Time difference between consecutive images is Δt = 0.01 s.

value. It is apparent that both pressures exhibit significant fluctuations, although characteristics of these fluctuations are unclear.

Towards this end, Fig. 3(b) provides a plot of the same two pressure measurements as Fig. 3(a), this time zoomed into focus on only the first two seconds. It is apparent from this plot that these pressure fluctuations are composed of at least two components, one manifest as low frequency, large amplitude oscillations, and the other as small amplitude, high frequency oscillations superimposed on the low frequency mode. It is also clear that the low frequency mode is not perfectly sinusoidal, especially in the case of the inlet pressure measurement, but is periodic nevertheless.

Fig. 3(c) further reinforces this by providing amplitude versus frequency plots for both inlet and outlet pressure signals, found by performing a fast Fourier transform on the 20-s duration transient pressure signals shown in Fig. 3(a). Both subplots show clear peak frequencies of oscillation in the 1–3 Hz range, with sharp peaks also present in the high (20–100 Hz) range, thus affirming the idea of a dominant low-frequency oscillatory mode with higher frequency oscillations superimposed first presented when analyzing Fig. 3(b).

The presence of this dominant low-frequency oscillatory mode can be tied back to the transient passage of HDFs observed in Fig. 2. In fact, by finding the time between successive HDFs in Fig. 2 and using the difference to calculate a single event frequency f_{SE}, Fig. 3 (d) shows that the peak frequencies of oscillation identified in Fig. 3(c) fall very close to the single event frequency associated with cyclical passage of HDFs observed in Fig. 2.

Although only calculated for a single case here, prior works [54,55] have included multiple calculations of single-event frequency for flow visualization images covering a range of operating conditions and found values are always similar to those seen when performing fast Fourier transforms of accompanying pressure measurements.

3.3. Density Wave Oscillation mechanism

Having identified the cyclical passage of High Density Fronts (HDFs) using flow visualization results and proved they are responsible for the dominant low-frequency pressure oscillations observed experimentally, it is necessary to provide a physical
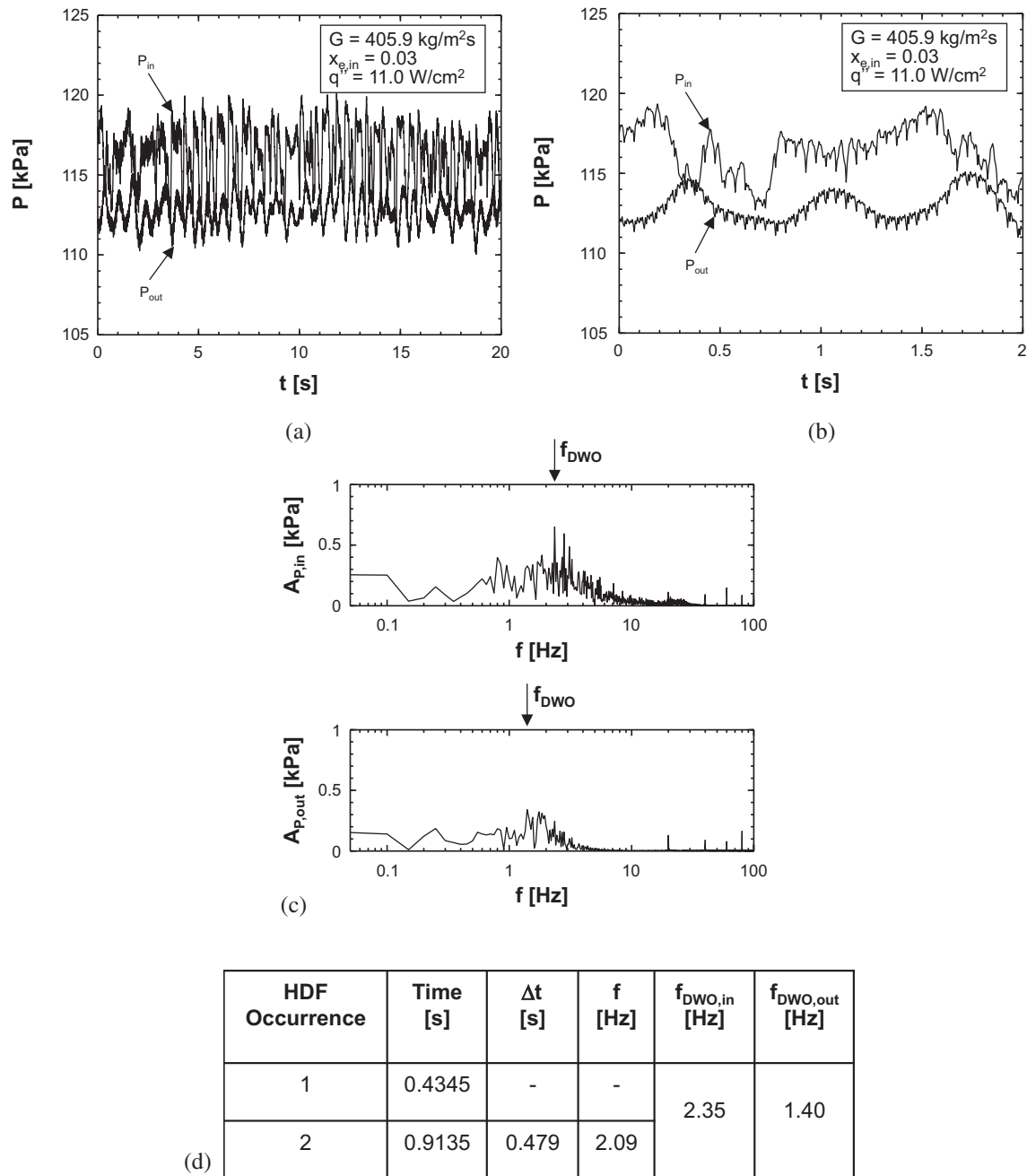
Fig. 3. Results for G = 405.9 kg/m²s, $x_{e,in}$ = 0.03, P_{in} = 116.4 kPa, and q'' = 11.0 W/cm²: (a) transient pressure data collected at inlet and outlet of FBM's heated length over 20-s period, (b) transient pressure data collected at inlet and outlet of FBM's heated length focused over 2-s period to highlight combined effects of high and low frequency oscillations, (c) amplitude versus frequency plots generated by fast Fourier transforms of signals in (a) with peak frequencies of oscillation identified, and (d) tabulated values of time at which high density fronts are observed in Fig. 2, along with associated single event frequency for comparison with peak frequencies observed in (c).

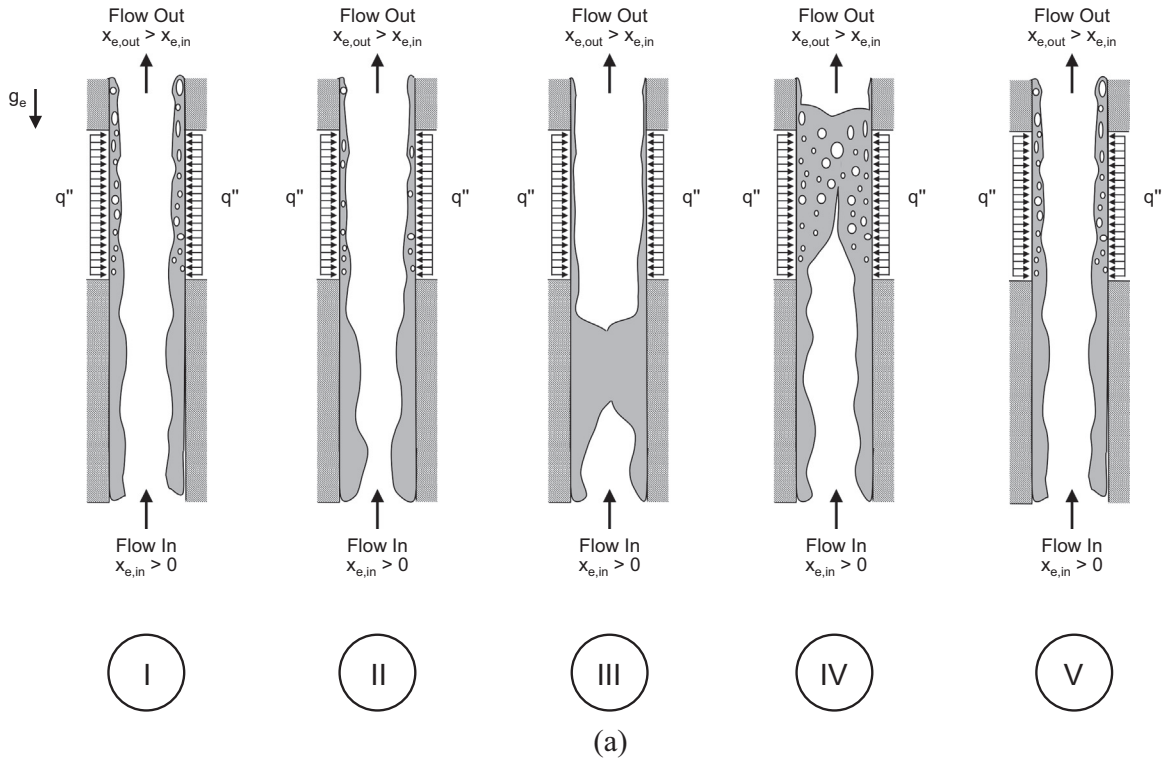description of the process by which DWOs manifest within the present system.

Fig. 4(a) provides a sequence of five schematics illustrating key stages of the phenomenon, and Fig. 4(b) contains descriptions of each. The nominal condition for the flow field is shown in stage I in Fig. 4(a), and is comprised of annular flow throughout the entire length of the channel, similar to that described when analyzing flow visualization results in Fig. 2.

Moving forward in time, stage II shows liquid accumulating in the upstream region of the channel, leading to reduced liquid content along the heated length (downstream portion of the test section). This accumulation of liquid in the upstream region can be attributed to the ~3 order of magnitude difference in the magnitude of body force acting on the liquid phase compared to that on the vapor phase. It should be noted that, during this process, mass inflow to the channel is assumed to remain constant, while mass outflow from the channel necessarily decreases due to the accumulation of liquid phase in the upstream portion of the channel.

Stage III shows that a point is reached at which liquid buildup in the inlet region leads to the formation of a HDF which travels along the length of the channel. The motion of the HDF is largely driven by the difference in momentum flux across the HDF itself, with high mass-velocity flow at the inlet of the channel impinging on

(a)

Stage	Description
I	In its initial state, annular co-current flow dominates throughout the length of the channel. Phase change occurs along the heated length due to energy provided by two sets of electric heaters mounted on opposite walls.
II	Due to the significant influence of body force on the liquid film compared to that on the vapor core, liquid film flow along the channel stagnates, and liquid begins accumulating towards the entrance region of the channel. This leads to reduced liquid content in the downstream portion of the channel, causing the liquid film along the heated length to begin to dry out.
III	As the liquid film thickness increases in the region upstream of the heated length, mass is no longer conserved within the channel. This is due to a disproportionate ratio of vapor to liquid exiting the channel, versus that entering the channel. In an effort to rectify the situation, the momentum of the accumulated liquid is increased by the difference in momentum flux between upstream and downstream regions, and it begins to move along the channel, re-wetting the walls in its wake. In this manner, the high density front (HDF) moves along the channel to ensure conservation of mass (on a time-averaged basis), re-wetting the liquid film in its wake. Just prior to the HDF reaching the heated length, the liquid film within the heated length is at its minimum thickness, and flow exiting the channel is almost entirely vapor.
IV	As the HDF passes through the heated length of the channel, re-wetting the heated walls, nucleation boiling is re-established. In the wake of the HDF liquid film, thickness is returned to nominal value and annular, co-current flow is reestablished. Flow exiting the channel is still mostly vapor, but the accumulated liquid (HDF) will soon pass, satisfying the hitherto violated conservation of mass.
V	HDF having exited the channel, the flow returns to its initial state of parallel, co-current annular flow throughout the channel length. Body force effects soon begin to dominate once more, however, and the cyclical formation of high density fronts continues. This cyclical process is how Density Wave Oscillations (DWOs) manifest within two-phase flow in mini/macro channels.

(b)

Fig. 4. (a) Schematics outlining cyclical process behind Density Wave Oscillations (DWOs), with (b) descriptions of key features present in each stage of the process.

the liquid accumulated in the upstream region, thus imparting momentum to the HDF. At the same time, the portion of the channel downstream of the HDF experiences near-total dryout, with only vapor flow exiting the channel.

Stage IV illustrates how, as the HDF moves along the channel, it acts to re-wet the liquid film along the walls and re-establish annular flow. As it passes out of the channel altogether, stage V shows annular flow re-established, leading to conditions similar to those of stage I from which the process may begin again.

This sequence of five stages, described mechanistically to provide an explanation for the cyclical passage of HDFs observed in

images and the associated pressure fluctuations seen in transient measurements and attributed to DWOs, provides a reasonable baseline from which to begin detailed modeling work.

4. Density Wave Oscillation (DWO) model development

Description of the model development will proceed in three steps: First, schematic presentations of key regions of interest and relevant physical processes occurring therein will be presented to illustrate how key elements of the mechanistic process

described in Fig. 4 may be quantified. Key assumptions used during modeling will also be discussed here.
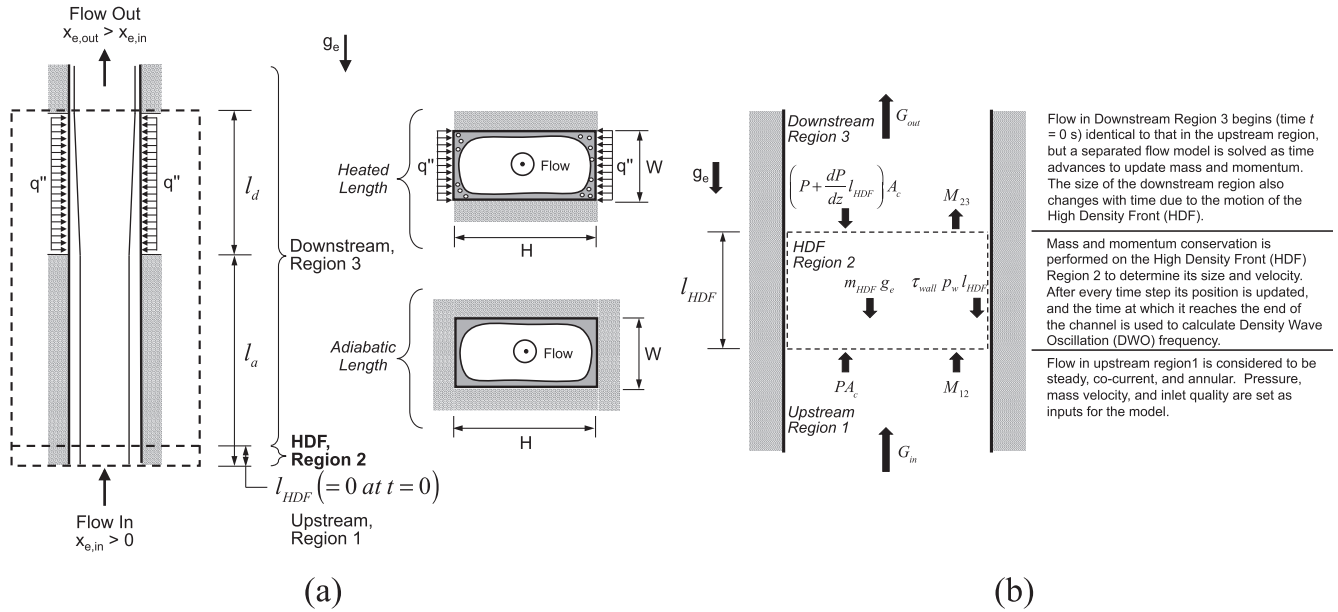
Second, a full solution process will be outlined, showing step by step how the model is solved to find parameters of interest (namely frequency and amplitude of DWO induced pressure oscillations). At this point all relevant constitutive relations will be provided, and any additional assumptions employed to ensure stable solutions discussed.

Finally, numeric results for model sub-components will be presented for select sub-cases to show how the model behaves in time as it approaches a solution.

4.1. Model setup and advancement

As shown in Fig. 4, the nominal flow condition for cases of interest here is that of annular, co-current flow. The model development will begin by considering flow through a rectangular channel to match the cross section of the FBM; the same model can tackle circular channels as well.

Fig. 5(a) provides schematics of the entire FBM under nominal conditions for the current investigation. The fluid length is separated into adiabatic and heated (diabatic) lengths, with liquid film thickness constant along the adiabatic length and linearly depen-
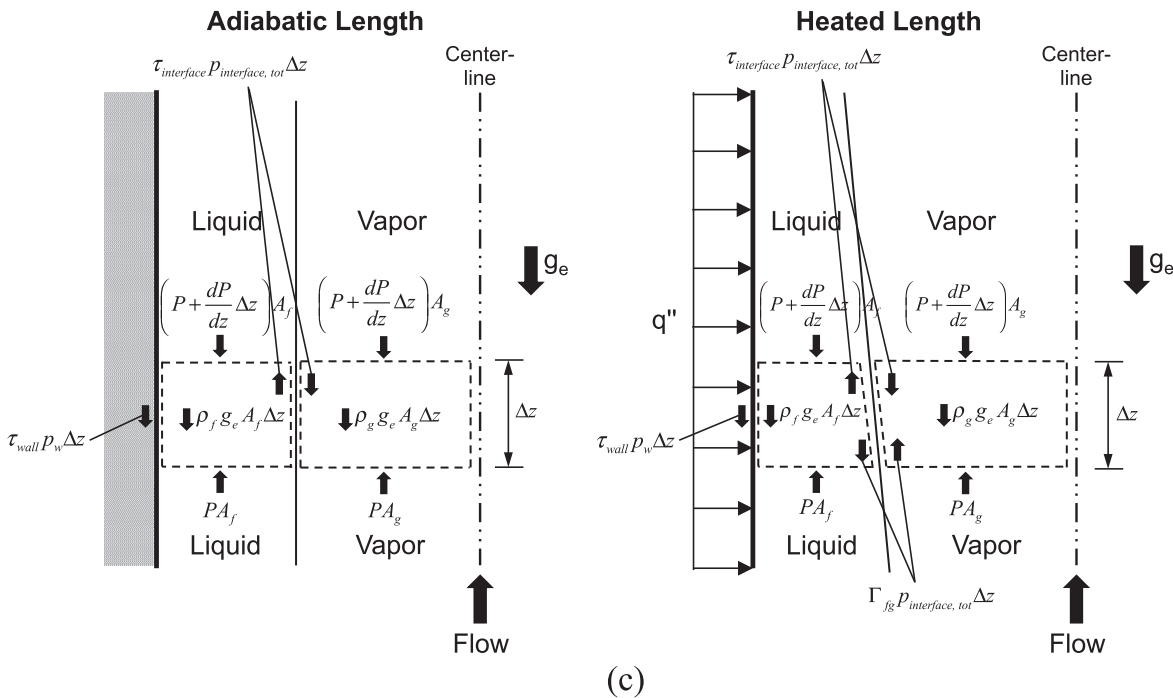

(a)

(b)

(c)

Fig. 5. (a) General model setup, key characteristics of which are presence of annular flow throughout, segmentation into Upstream Region 1, High Density Front Region 2, and Downstream Region 3, and separate adiabatic and diabatic lengths. (b) Control-volume encompassing HDF Region. (c) Depiction of force terms in separated flow model used in Downstream Region 3.

dent on position in the heated length due to the application of a uniform, constant heat flux along the heated length. Cross section schematics for both portions of the channel are also provided.

Fig. 5(a) also establishes three distinct regions for analysis:

(1) Region 1, Upstream: This section is used to describe flow entering the channel, and is assumed to be steady, with flow field parameters determined by nominal (time-averaged) operating conditions for each test case.

(2) Region 2, High Density Front (HDF): Shown in Fig. 5(a) as a thin region segregating Region 1 (Upstream) from Region 3 (Downstream). It will be discussed in more detail when analyzing Fig. 5(b).

(3) Region 3, Downstream: Flow in the downstream region is initially ($t = 0$ s) assumed to possess the same mass flow rate as Region 1, with the same quality along the adiabatic length and a linear variation in quality along the heated length. As time advances, however, a separated flow model is solved to update mass and momentum (with conservation of energy also used to account for phase change) in this portion of the channel. This allows the potential for liquid to accumulate in Region 2 should the flow model predict instantaneous mass velocity entering the channel (assumed to be constant) to be greater than that exiting (determined by solution of the separated flow model).

More detail will be provided on Regions 2 and 3 in subsequent figures.

Fig. 5(b) provides a schematic of Region 2, corresponding to the HDF. A key parameter in this schematic is the length of the HDF, l_{HDF}, defined as

$$l_{HDF} = \frac{m_{HDF}}{A_c \rho_f},$$ (3)

where m_{HDF} is the mass stored in the HDF, A_c the cross-sectional area of the channel, and ρ_f the density of liquid evaluated at the inlet pressure. It should be noted here that, for modeling purposes, the HDF is considered to be composed entirely of liquid, although in reality some amount of vapor is typically present depending on operating conditions.

At the onset of the simulation m_{HDF} is equal to zero, meaning the length of the HDF is zero and no conservation equations are solved for the Region 2 control-volume. As time is advanced and the separated flow model is solved for Region 3, mass outflow from the channel begins to drop below mass inflow, meaning mass must be stored within the channel. As mentioned when presenting Fig. 4, mass storage within the channel is accomplished through liquid phase accumulation in the near-inlet region, here translating to increasing values of m_{HDF} and l_{HDF}. Once it possesses finite size and mass, it is possible to solve conservation of momentum for the Region 2 control-volume to find important parameters including HDF velocity, u_{HDF}, and pressure drop across the HDF, ΔP_{HDF}.

Conservation of momentum for the HDF includes terms corresponding to pressure drop, body force, viscous shear, and differences in momentum between Regions 1 and 2 (upstream and

Table 2
Relevant assumptions, relations, and references for Region 2 control volume.

Key assumptions	(1) HDF is entirely composed of liquid (2) HDF initially has no mass, no velocity (3) Neglect interfacial curvature at front and back of HDF (surface tension effects) (4) Neglect virtual mass force effects (5) Neglect loss of liquid from HDF while re-wetting walls (6) Neglect property changes due to local pressure changes (7) Limit relative velocities to ≥ 0
Constitutive relations	$M_{12}^n = \rho_g A_{g,tot}^0 (u_g^0 - u_{HDF}^n)^2 + \rho_f A_{f,tot}^0 (u_f^0 - u_{HDF}^n)^2$ $M_{23}^n = \rho_g A_{g,tot}^n (u_g^n - u_{HDF}^n)^2 + \rho_f A_{f,tot}^0 (u_f^n - u_{HDF}^n)^2$ $\tau_{wall}^n = \frac{3\mu_f u_{HDF}^n}{D_H}$ $\Delta P_{HDF}^n = \frac{f_{HDF}^n (1.5 G_{in})^2 l_{HDF}^n}{2\rho_f D_H} + \rho_f g l_{HDF}^n$ where 0 indicates initial conditions and n current time step
References	Friction factor f_{HDF} is determined using the Colebrook-White equation for turbulent flow [99] with roughness of $\varepsilon = 0.000508$ m for polished polycarbonate

Table 3
Relevant assumption, relations, and references for Region 3 control volumes.

Key assumptions	(1) Flow conditions initially identical to those in Region 1 (2) Neglect property changes due to local pressure differences (3) Use lumped analysis for region (parameters are not a function of space in Region 3, instantaneous inflow is equal to outflow) (4) Neglect interfacial curvature and associated effects (5) Flow qualities limited to the range $0.01 \leqslant x_{ave,tot} \leqslant 0.99$ to prevent division by zero (6) Phase momentums are limited to the range $0 < M_k < M_{k,1}$, where the subscript k indicates each respective phase and 1 refers to their region 1 values
Constitutive relations	$\tau_{wall}^n = \frac{\rho_f f_w^n u_f^{n2}}{2}$ $\tau_{interface}^n = \frac{f_i^n \rho_g (u_g^n - u_i^n)^2 + (u_g^n - u_i^n)\frac{q''}{h_{fg}}}{2}$ $\left(\frac{dP}{dz}\right)^n = \left(\frac{dP}{dz}\right)_{2\phi}^n = \left(\frac{dP}{dz}\right)_A^n + \left(\frac{dP}{dz}\right)_G^n + \left(\frac{dP}{dz}\right)_F^n$ $\Gamma_{fg}^n = \frac{q'' u_{interface}^n}{h_{fg}}$
References	– Friction factor f_w, is determined using the Colebrook-White equation for turbulent flow [99] with roughness of $\varepsilon = 0.000508$ m for polished polycarbonate – Interfacial shear stress is determined by the Wallis relation [100] – Frictional pressure drop is calculated using the Homogeneous Equilibrium Model with the mixture viscosity model of Akers et al. [101]

HDF) and Regions 2 and 3 (HDF and downstream). The full form of each momentum component is provided in Table 2, along with references for relevant constitutive relations, key assumptions, and related comments. It should be noted here that the relationship used to find wall shear stress acting on the HDF comes from directly evaluating $\mu_f(du_{HDF}/dy)$, using a linear fit for velocity ranging from $u = 0$ at the channel wall to $u = 1.5u_{HDF}$ at the channel centerline (where u_{HDF} is the average HDF velocity calculated by the model).

Prior to discussing the method by which the model accounts for the motion of the HDF along the channel in time, it is first necessary to provide some discussion on the separated flow model being solved in the downstream portion of the channel, Region 3. Fig. 5(c) provides schematics of control volumes for both liquid and vapor phases in adiabatic and diabatic portions of the channel, with key force components defined in each, including pressure drop, wall shear stress, interfacial shear stress, body force, and momentum transfer due to phase change. Similar to what was done with the HDF control volume, the full form of all terms can be found in Table 3, along with references for relevant constitutive relations, key assumptions, and related comments.

Having defined the relevant physical processes in play, Fig. 6(a) illustrates how they come together to form an overall system with the goal of finding the size and velocity of the HDF at any given instant in time. Starting with Region 3, conversation of momentum is updated at each time step, with values used to calculate new phase velocities. These velocities are then used to calculate the overall mass velocity in the downstream region at each instant in time.

This information is then used to update the mass stored in Region 2, the HDF. After this conservation of momentum is performed on Region 2 to find the updated velocity of the HDF, which can be multiplied by the time step Δt to find the updated z-location of the HDF at time n.

Fig. 6(b) illustrates this process by providing system schematics at four different times. Similar to the schematic presented in Fig. 5 (a), Fig. 6(b) shows that the model begins with Region 3 covering the entire downstream portion of the channel, and the HDF (Region 2) possessing zero thickness. As time advances, the HDF grows in length (due to mass accumulating within) and travels along the length of the channel, causing Region 3 to decrease in length. It should be noted that everything upstream of the HDF is assumed to follow the behavior of Region 1, which physically corresponds to passage of the HDF serving to re-wet the liquid film and re-establish annular, co-current flow throughout (as seen in Fig. 2).

As the HDF continues to travel along the channel length, Fig. 6 (b) shows the adiabatic length eventually going to zero, and the
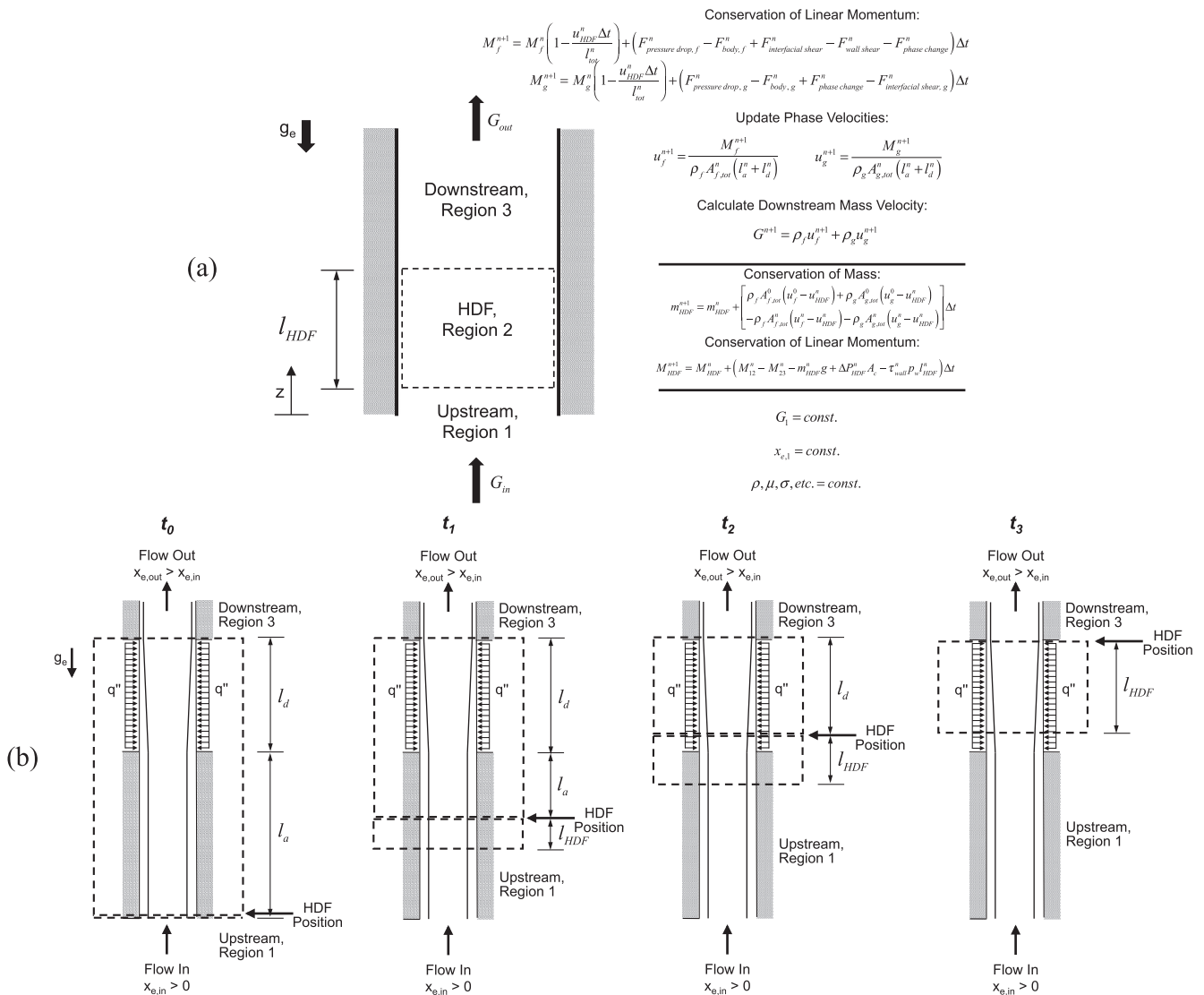

Fig. 6. (a) Depiction of primary solution equations for each region of the DWO model, and (b) evolution of model control volumes with time.

model concludes when the HDF reaches the end of the channel. At this point, the total time taken for the HDF to accumulate mass and travel to the end of the channel is defined here as the period of Density Wave Oscillation (DWO), allowing a frequency to be calculated as

$$f_{DWO} = \frac{1}{t_{HDF\ exits\ channel}}. \tag{4}$$

Similarly, amplitude of DWO induced pressure oscillations may be calculated at the same instant by taking one-half the difference between maximum total two-phase and frictional HDF pressure drops, or

$$A_{DWO} = \frac{\Delta P^0_{2\phi,max} - \Delta P^n_{HDF,\ max\ frictional}}{2}, \tag{5}$$

where maximum two-phase pressure drop is calculated at time $t = 0$ s for the entire channel and maximum HDF pressure drop is calculated at the final time-step. These terms reflect the difference in pressure drop in the channel under nominal operating conditions ($\Delta P_{2\phi}$), evaluated at time $t = 0$ s in the model when conditions in Region 3 are identical to those in Region 1, and when the HDF is passing through the heated length (ΔP_{HDF}), evaluated at time $t = t_{final}$ when the HDF is at its maximum length and is passing from the channel. Relations used for the calculation of each pressure drop term will be provided when discussing the full solution procedure in the following section. It should be noted, however, that selection of the relationship for two-phase pressure drop was performed using extensive analysis on accuracy of two-phase frictional pressure drop correlations presented in a prior study by the present authors [53].

The general idea behind this formulation is that channel pressure drop characteristics change in response to the alternating passage of two-phase annular flow and a single-phase slug, meaning just as the frequency at which DWOs are observed is related to the time required for the downstream region to cycle through annular two-phase flow, dryout, single-phase liquid (HDF), and return to annular two-phase flow, the magnitude of associated pressure oscillations are tied to the changes in pressure drop encountered while cycling from a maximum pressure drop regime (annular two-phase flow) to a minimal pressure drop regime (single-phase liquid).

4.2. Full solution procedure

Fig. 7 provides a flow chart for solution of the current model, and a full list of relationships necessary for replicating the model may be found in Table 4 (with each row corresponding to the indicated step in Fig. 7). Important geometric parameters defined in Table 4 include length l, flow cross-sectional area A occupied by each phase, perimeter p (including diabatic, interfacial, and wetted variants), and vapor-core radius r_g (calculated assuming a circular shape). Key subscripts used when describing these and other parameters this section include a for adiabatic, d for diabatic, tot for total (indicated the parameter is evaluated along the entire length of Region 3), z to indicate streamwise position (primarily used when evaluating two-phase pressure drop by marching along the channel length), 2φ to indicate two-phase, w for wetted, and *interface* for interfacial terms. Key subscripts on force terms include *wall shear* for wall shear stress, *interfacial shear* for interfacial shear stress, *pressure drop*, for pressure drop evaluated for phase k ($k = f$ or $k = g$), *phase change* for momentum transfer due to phase change, and *body*, for body force evaluated for phase k.

Fig. 7 indicates the model starts by collecting relevant input parameters, including test section geometry and flow-field conditions for Region 1 (namely pressure P_{in}, quality $x_{e,in}$, heat flux along the heated length q'', and mass velocity G_{in}). All relevant fluid properties are calculated at the prescribed inlet pressure P_{in}, and assumed to remain constant during model advancement. This is a reasonable assumption, as analysis of experimental amplitude of DWO induced pressure fluctuations reveals they do not exceed 7% of time-averaged pressure in magnitude, meaning any accompanying property fluctuations will be minimal [55].

Model inputs for Region 1 are used to calculate initial values of all important flow-field parameters in Region 3, including adiabatic and diabatic length average qualities $x_{ave,a}$ and $x_{ave,d}$, respectively, phase velocities u_f and u_g, phase flow areas A_f and A_g, phase momentums M_f and M_g and phase mass velocities G_f and G_g.

A key parameter in calculating flow-field variables is void fraction α, which due to its difficulty to measure experimentally is approximated here using the Zivi void fraction correlation [102], defined as

$$\alpha_{Zivi} = \left(1 + \left(\frac{1-x}{x} \right) \left(\frac{\rho_g}{\rho_f} \right)^{2/3} \right)^{-1}, \tag{6}$$

where x is flow quality evaluated over the region of interest.

Having initialized all relevant parameters in Region 3, force terms outlined in Fig. 5(c) may be calculated, and momentum updated for Region 3. It is important to note that the equation handling conservation of momentum for Region 3 includes a term to account for changing length of the control volume due to HDF motion along the channel.

Updated momentum values are then used to find updated phase velocities in Region 3, which in turn allow calculation of overall mass velocity in Region 3 at the current time step. This value is used along with the known, constant value of mass velocity entering the channel (Region 1) to update conservation of mass for the HDF (Region 2).

It is important to note here that conservation of momentum for the HDF is not solved (meaning it is assumed to remain at rest) until it has accumulated mass equal to 0.0005 kg (0.5 g). This is intended to avoid false prediction of extremely high accelerations in the initial time steps.

After updating mass and momentum for the HDF (Region 2), updates for velocity and stream-wise location of the HDF may also be made. As long as the HDF has not reached the end of the channel, the model continues to run by first updating important flow field parameters, advancing to the next time step, and repeating the process.

A particular challenge in the development of the present model is updating flow quality in the downstream portion of the channel. Quality is used to find void fraction (via Eq. (6)), which is in turn used to calculate flow areas and interfacial perimeter to be used in conservation of momentum. This makes it a critical component of the model, one which must be treated with care.

Beginning with values from the previous time step, quality in Region 3 is updated through linear superposition of four key effects along each portion of the channel length (adiabatic and diabatic):

(1) Preservation of average quality for each length from the previous time step.
(2) Inflow of a new flow quality $x_{f,in}^{n+1}$ to the initial length (adiabatic while $z_{HDF}^{n+1} < l_a^0$, diabatic after) calculated based on updated phase velocities and advected into length at the mean of the two phase velocities. Similarly, if $z_{HDF}^{n+1} < l_a^0$, there is inflow of adiabatic length average quality $x_{a,ave}^n$ into the diabatic length at the same velocity.
(3) Outflow of old average quality for each length at the same average velocity. Outflow from the adiabatic length is inflow to the diabatic length, and outflow from the diabatic length exits the channel.
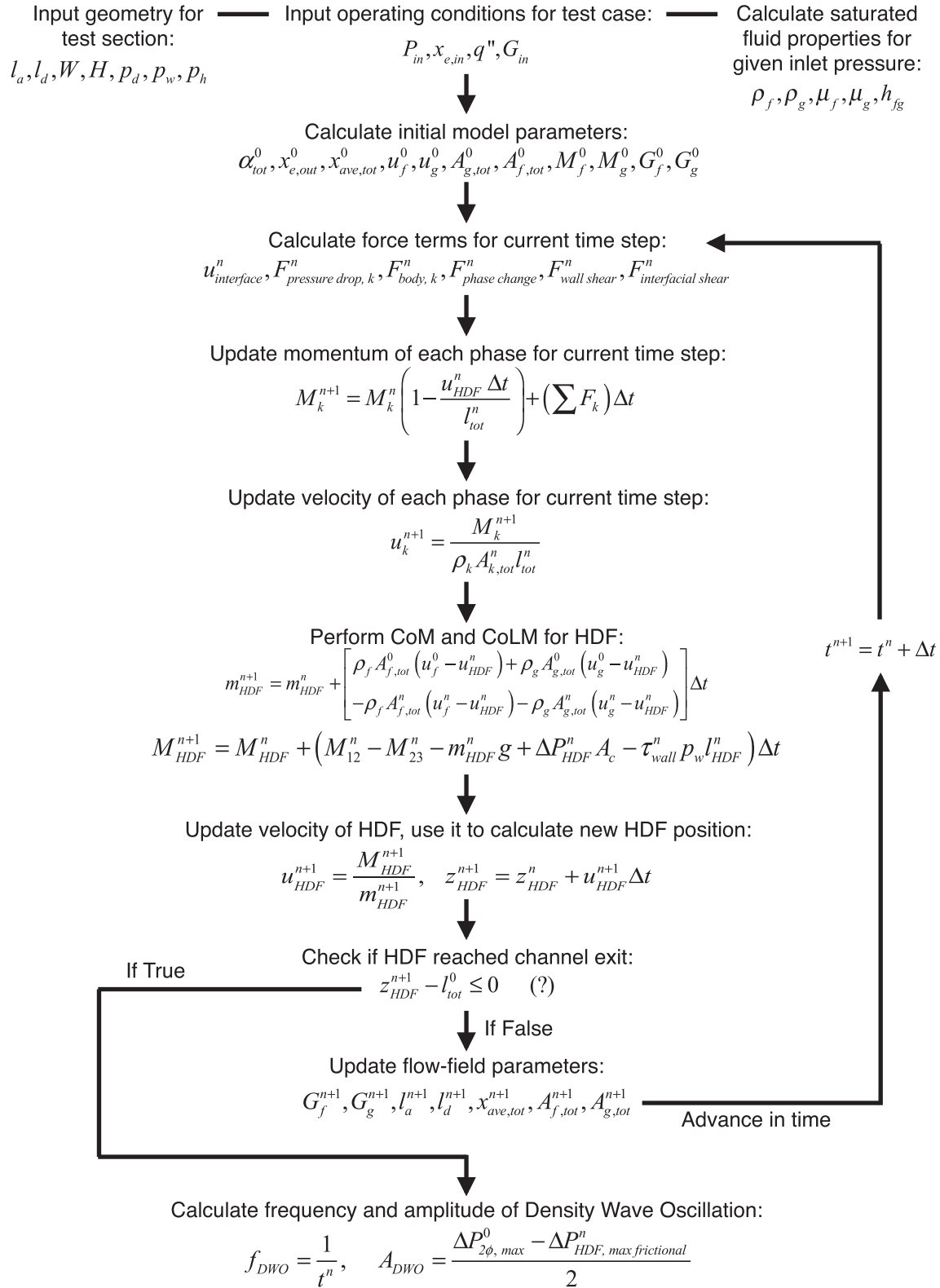
Input geometry for test section:

$$l_a, l_d, W, H, p_d, p_w, p_h$$

Input operating conditions for test case:

$$P_{in}, x_{e,in}, q'', G_{in}$$

Calculate saturated fluid properties for given inlet pressure:

$$\rho_f, \rho_g, \mu_f, \mu_g, h_{fg}$$

Calculate initial model parameters:

$$\alpha_{tot}^0, x_{e,out}^0, x_{ave,tot}^0, u_f^0, u_g^0, A_{g,tot}^0, A_{f,tot}^0, M_f^0, M_g^0, G_f^0, G_g^0$$

Calculate force terms for current time step:

$$u_{interface}^n, F_{pressure\ drop,\ k}^n, F_{body,\ k}^n, F_{phase\ change}^n, F_{wall\ shear}^n, F_{interfacial\ shear}^n$$

Update momentum of each phase for current time step:

$$M_k^{n+1} = M_k^n \left(1 - \frac{u_{HDF}^n \Delta t}{l_{tot}^n} \right) + \left(\sum F_k \right) \Delta t$$

Update velocity of each phase for current time step:

$$u_k^{n+1} = \frac{M_k^{n+1}}{\rho_k A_{k,tot}^n l_{tot}^n}$$

Perform CoM and CoLM for HDF:

$$m_{HDF}^{n+1} = m_{HDF}^n + \begin{bmatrix} \rho_f A_{f,tot}^0 \left(u_f^0 - u_{HDF}^n \right) + \rho_g A_{g,tot}^0 \left(u_g^0 - u_{HDF}^n \right) \\ -\rho_f A_{f,tot}^n \left(u_f^n - u_{HDF}^n \right) - \rho_g A_{g,tot}^n \left(u_g^n - u_{HDF}^n \right) \end{bmatrix} \Delta t$$

$$M_{HDF}^{n+1} = M_{HDF}^n + \left(M_{12}^n - M_{23}^n - m_{HDF}^n g + \Delta P_{HDF}^n A_c - \tau_{wall}^n p_w l_{HDF}^n \right) \Delta t$$

Update velocity of HDF, use it to calculate new HDF position:

$$u_{HDF}^{n+1} = \frac{M_{HDF}^{n+1}}{m_{HDF}^{n+1}}, \quad z_{HDF}^{n+1} = z_{HDF}^n + u_{HDF}^{n+1} \Delta t$$

Check if HDF reached channel exit:

$$z_{HDF}^{n+1} - l_{tot}^0 \leq 0 \quad (?)$$

If True

If False

Update flow-field parameters:

$$G_f^{n+1}, G_g^{n+1}, l_a^{n+1}, l_d^{n+1}, x_{ave,tot}^{n+1}, A_{f,tot}^{n+1}, A_{g,tot}^{n+1}$$

$$t^{n+1} = t^n + \Delta t$$

Advance in time

Calculate frequency and amplitude of Density Wave Oscillation:

$$f_{DWO} = \frac{1}{t^n}, \quad A_{DWO} = \frac{\Delta P_{2\phi,\ max}^0 - \Delta P_{HDF,\ max\ frictional}^n}{2}$$

Fig. 7. Flow chart for model solution.

(4) Phase change along the heated length of the channel.

Altogether this provides the following relationships for updated qualities along the adiabatic and diabatic lengths, respectively, of

$$x_{ave,a}^{n+1} = \frac{\frac{1}{2} x_{f,in}^{n+1} (u_g^{n+1} + u_f^{n+1}) \Delta t - \frac{1}{2} x_{ave,a}^n (u_g^{n+1} + u_f^{n+1}) \Delta t + x_{ave,a}^n l_a^{n+1}}{l_a^{n+1}}$$

(7)

Table 4
Model relationships associated with each respective step in the model solution procedure outlined in Fig. 7.

Calculate initial model parameters	$\alpha_{Zivi}(x_e) = \left(1 + \left(\frac{1-x_e}{x_e}\right)\left(\frac{\rho_g}{\rho_f}\right)^{2/3}\right)^{-1}$, $x^0_{e,out} = x^0_{e,in} + \frac{q''p_H l_d}{G_{in}A_c h_{fg}}$, $x^0_{ave,a} = x^0_{e,in}$, $x^0_{ave,d} = \frac{x^0_{e,in}+x^0_{e,out}}{2}$, $x^0_{ave,tot} = \frac{x^0_{ave,a}l^0_a + x^0_{ave,d}l^0_d}{l^0_a + l^0_d}$, $\alpha^0_{tot} = \alpha_{Zivi}(x^0_{ave,tot})$, $A^0_{g,tot} = A_c\alpha^0_{tot}$, $A^0_{f,tot} = A_c - A^0_{g,tot}$, $\alpha^0_{in} = \alpha_{Zivi}(x^0_{e,in})$, $l^0_{tot} = l^0_a + l^0_d$, $r^0_g = \sqrt{\frac{A^0_{g,tot}}{\pi}}$, $p^0_{interface,tot} = 2\pi\sqrt{\frac{A^0_{g,tot}}{\pi}}$, $u^0_g = \frac{G_{in}x^0_{e,in}}{\rho_g\alpha^0_{in}}$, $u^0_f = \frac{G_{in}(1-x^0_{e,in})}{\rho_f(1-\alpha^0_{in})}$, $M^0_f = \rho_f u^0_f A^0_{f,tot} l^0_{tot}$, $M^0_g = \rho_g u^0_g A^0_{g,tot} l^0_{tot}$
Force terms for current time step	$u^n_{interface} = \frac{u^n_f\rho_f + u^n_g\rho_g}{\rho_f + \rho_g}$, $F^n_{pressure\,drop,k} = -\left(\sum_{z=0}^{l_{tot}}\left(\frac{dP}{dz}\right)^n_{2\phi,z}\Delta z\right)A^n_{k,tot}$, $F^n_{body,k} = \rho_k g\, A^n_{k,tot} l^n_{tot}$, $F^n_{phase\,change} = \left(\frac{q''p_d l^n_d}{h_{fg}}\right)u^n_{interface}$, $F^n_{wall\,shear} = \frac{\rho_f f^n_w u^{n2}_f p_w l^n_{tot}}{2}$, $F^n_{interfacial\,shear} = \frac{f^n_i\rho_g(u^n_g - u^n_{interface})^2 p^n_{interface,tot} l^n_{tot} + (u^n_g - u^n_{interface})\frac{q''p_d l^n_d}{h_{fg}}}{2}$, $f^n_w = \frac{64}{Re^n_f}$ for $Re^n_f \leqslant 2300$ $\frac{1}{\sqrt{f^n_w}} = -2\log\left(\frac{\varepsilon}{3.7D_H} + \frac{2.51}{Re^n_f\sqrt{f^n_w}}\right)$ for $Re^n_f > 2300$ $Re^n_f = \frac{\rho_f u^n_f D_H}{\mu_f}$ $f^n_i = \frac{16}{Re^n_c}$ for $Re^n_c \leqslant 2000$ $f^n_i = \frac{0.079}{(Re^n_c)^{0.25}}$ for $2000 < Re^n_c \leqslant 20,000$ $f^n_i = \frac{0.046}{(Re^n_c)^{0.2}}$ for $20,000 < Re^n_c$ $Re^n_c = \frac{\rho_g(u^n_g - u^n_{interface})r^n_g}{\mu_g}$ $\left(\frac{dP}{dz}\right)^n_{2\phi,z} = \left(\frac{dP}{dz}\right)^n_{A,z} + \left(\frac{dP}{dz}\right)^n_{F,z} + \left(\frac{dP}{dz}\right)^n_{G,z}$, $\alpha_z = \left(1 + \frac{1-x_z}{x_z}\frac{\rho_g}{\rho_f}\right)^{-1}$, $-\left(\frac{dP}{dz}\right)^n_{A,z} = G^{n2}\frac{d}{dz}\left[\frac{v_g x^2_z}{\alpha_z} + \frac{v_f(1-x_z)^2}{1-\alpha_z}\right]$, $-\left(\frac{dP}{dz}\right)^n_{G,z} = (\alpha_z\rho_g + (1-\alpha_z)\rho_f)g$, $-\left(\frac{dP}{dz}\right)^n_{F,z} = \left[\frac{2f^n_{2\phi,z}v_f G^{n2}}{D_H}\right]\left(1 + x_z\frac{v_g - v_f}{v_f}\right)$, $f^n_{2\phi,z} = \frac{16}{Re^n_{2\phi,z}}$, $Re^n_{2\phi,z} < 2000$ $f^n_{2\phi,z} = \frac{0.079}{(Re^n_{2\phi,z})^{0.25}}$, $2000 \leqslant Re^n_{2\phi,z} < 20,000$ $f^n_{2\phi,z} = \frac{0.046}{(Re^n_{2\phi,z})^{0.2}}$, $20,000 \leqslant Re^n_{2\phi,z}$ $Re^n_{2\phi,z} = \frac{G^n D_H}{\mu_{2\phi,z}}$, $\mu_{2\phi,z} = \frac{\mu_f}{(1-x_z)+x_z\left(\frac{v_g}{v_f}\right)^{0.5}}$
Update phase momentum and velocity	$M^{n+1}_f = M^n_f\left(1 - \frac{u^n_{HDF}\Delta t}{l^n_{tot}}\right) + (F^n_{pressure\,drop,f} - F^n_{body,f} - F^n_{phase\,change} - F^n_{wall\,shear} + F^n_{interfacial\,shear})\Delta t$, $M^{n+1}_g = M^n_g\left(1 - \frac{u^n_{HDF}\Delta t}{l^n_{tot}}\right) + (F^n_{pressure\,drop,g} - F^n_{body,g} + F^n_{phase\,change} - F^n_{interfacial\,shear})\Delta t$, $u^{n+1}_f = \frac{M^{n+1}_f}{\rho_f A^n_{f,tot} l^n_{tot}}$, $u^{n+1}_g = \frac{M^{n+1}_g}{\rho_g A^n_{g,tot} l^n_{tot}}$
Update mass, momentum, velocity, length, and position of HDF	$m^{n+1}_{HDF} = m^n_{HDF} + [\rho_f A^0_{f,tot}(u^0_f - u^n_{HDF}) + \rho_g A^0_{g,tot}(u^0_g - u^n_{HDF}) - \rho_f A^n_{f,tot}(u^n_f - u^n_{HDF}) - \rho_g A^n_{g,tot}(u^n_g - u^n_{HDF})]\Delta t$, $M^{n+1}_{HDF} = M^n_{HDF} + \left(\begin{array}{l}\rho_g A^0_{g,tot}(u^0_g - u^n_{HDF})^2 + \rho_f A^0_{f,tot}(u^0_f - u^n_{HDF})^2 - \rho_g A^n_{g,tot}(u^n_g - u^n_{HDF})^2 \\ -\rho_f A^n_{f,tot}(u^n_f - u^n_{HDF})^2 - m^{n+1}_{HDF}g + \Delta P^n_{HDF}A_c - \frac{3\mu_f u^n_{DWO}p_F l^n_{HDF}}{D_H}\end{array}\right)\Delta t$, $\Delta P^n_{HDF} = \frac{f^n_{HDF}(1.5G_{in})^2 l^n_{HDF}}{2\rho_f D_H} + \rho_f g l^n_{dwo}$, $l^{n+1}_{HDF} = \frac{m^{n+1}_{HDF}}{\rho_f A_c}$, $u^{n+1}_{HDF} = \frac{M^{n+1}_{HDF}}{m^{n+1}_{HDF}}$, $z^{n+1}_{HDF} = z^n_{HDF} + u^{n+1}_{HDF}\Delta t$, $f^n_{HDF} = \frac{64}{Re^n_{HDF}}$ for $Re^n_{HDF} \leqslant 2300$ $\frac{1}{\sqrt{f^n_{HDF}}} = -2\log\left(\frac{\varepsilon}{3.7D_H} + \frac{2.51}{Re^n_{HDF}\sqrt{f^n_{HDF}}}\right)$ for $Re^n_{HDF} > 2300$ $Re^n_{HDF} = \frac{G_{in}D_H}{\mu_f}$
Update flow-field parameters if HDF has not reached channel exit	$G^{n+1} = G^{n+1}_f + G^{n+1}_g = \frac{\rho_f u^{n+1}_f A^n_{f,tot} + \rho_g u^{n+1}_g A^n_{g,tot}}{A_c}$, $x^{n+1}_{f,in} = \frac{\rho_g u^{n+1}_g A^n_{g,tot}}{G^{n+1}A_c}$, if $z^{n+1}_{HDF} < l^0_a$: $l^{n+1}_a = l^0_a - z^{n+1}_{HDF}$, $x^{n+1}_{ave,a} = \frac{\frac{1}{2}x^{n+1}_{f,in}(u^{n+1}_g + u^{n+1}_f)\Delta t - \frac{1}{2}x^n_{ave,a}(u^{n+1}_g + u^{n+1}_f)\Delta t + x^n_{ave,a}l^{n+1}_a}{l^{n+1}_a}$ $x^{n+1}_{ave,d} = \frac{\frac{1}{2}x^n_{ave,a}(u^{n+1}_g + u^{n+1}_f)\Delta t - \frac{1}{2}x^n_{ave,d}(u^{n+1}_g + u^{n+1}_f)\Delta t + x^n_{ave,d}l^{n+1}_d + \frac{q''p_d l^{n+1}_d\Delta t}{l^{n+1}_d A^n_{d,f}\rho_f h_{fg}}}{l^{n+1}_d}$ if $z^{n+1}_{HDF} \geqslant l^0_a$: $l^{n+1}_a = 0$, $l^{n+1}_d = l^n_d - (z^{n+1}_{HDF} - l^0_a)$, $x^{n+1}_{ave,a} = 0$, $x^{n+1}_{ave,d} = \frac{\frac{1}{2}x^{n+1}_{f,in}(u^{n+1}_g + u^{n+1}_f)\Delta t - \frac{1}{2}x^n_{ave,d}(u^{n+1}_g + u^{n+1}_f)\Delta t + x^n_{ave,d}l^{n+1}_d + \frac{q''p_d l^{n+1}_d\Delta t}{l^{n+1}_d A^n_{d,f}\rho_f h_{fg}}}{l^{n+1}_d}$ Then: $x^{n+1}_{ave,tot} = \frac{x^{n+1}_{ave,a}l^{n+1}_a + x^{n+1}_{ave,d}l^{n+1}_d}{l^{n+1}_a + l^{n+1}_d}$, $\alpha^{n+1}_d = \alpha_{Zivi}(x^{n+1}_{ave,d})$, $A^{n+1}_{d,f} = (1 - \alpha^{n+1}_d)A_c$, $\alpha^{n+1}_{tot} = \alpha_{Zivi}(x^{n+1}_{ave,tot})$, $A^{n+1}_{g,tot} = \alpha^{n+1}_{tot}A_c$, $A^{n+1}_{f,tot} = (1 - \alpha^{n+1}_{tot})A_c$, $r^{n+1}_g = \sqrt{\frac{A^{n+1}_{g,tot}}{\pi}}$, $p^{n+1}_{interface,tot} = 2\pi\sqrt{\frac{A^{n+1}_{g,tot}}{\pi}}$
If HDF has reached channel exit, calculate associated amplitude and frequency	$f_{DWO} = \frac{1}{t^n}$, $A_{DWO} = \frac{\Delta P^n_{2\phi,max} - \Delta P^n_{HDF,maxfrictional}}{2}$

and

$$x_{ave,d}^{n+1} = \frac{\frac{1}{2}x_{ave,a}^n(u_g^{n+1}+u_f^{n+1})\Delta t - \frac{1}{2}x_{ave,d}^n(u_g^{n+1}+u_f^{n+1})\Delta t + x_{ave,d}^n l_d^{n+1} + \frac{q''p_d l_d^{n+1}\Delta t}{l_d^{n+1}A_{d,f}^n \rho_f h_{fg}}}{l_d^{n+1}},$$

(8)

with channel average quality then calculated as

$$x_{ave,tot}^{n+1} = \frac{x_{ave,a}^{n+1}l_a^{n+1} + x_{ave,d}^{n+1}l_d^{n+1}}{l_a^{n+1} + l_d^{n+1}}.$$

(9)

After the HDF passes through the entire adiabatic length $(z_{HDF}^{n+1} \geqslant l_a^0)$, the adiabatic length quality is set to zero (as it no longer affects the solution; in reality the adiabatic length is now composed partially by the HDF, with the remainder experiencing flow conditions identical to those in Region 1) and only the diabatic length quality is solved for.

This solution process continues until the HDF reaches the end of the channel $(z_{HDF}^{n+1} \geqslant l_a^0 + l_d^0)$, at which point frequency and amplitude of pressure fluctuations associated with its passage may be calculated.

4.3. Investigation of model sub-component trends

Having established all key relations used in model development and outlined the solution procedure, plots of these values versus time can be analyzed to determine physical validity of the model as a whole. Towards this end, Fig. 8 provides plots of important model components for Region 3 versus time for the case of mass velocity $G = 835.9$ kg/m^2 s, inlet pressure $P_{in} = 122$ kPa, inlet quality $x_{e,in} = 0.04$, and FBM heat flux $q'' = 2.5$ W/cm^2. It should be noted here that all model predictions shown hereafter were generated using a time step of $\Delta t = 0.0001$ s.

Fig. 8(a) and (b) shows plots of liquid and vapor phase momentum components versus time, along with the summation of these values (which is multiplied by Δt at each time step to update momentum for each phase). A key point to note is the dominance of body force over the initial ~0.05 s for the liquid phase, acting to drive the summation of force terms negative (thus reducing liquid phase momentum).

For the vapor phase in Fig. 8(b), interfacial shear is the dominant negative term, but overall vapor phase momentum is seen to increase due to the role of two-phase pressure drop.

In both Fig. 8(a) and (b) momentum balance components are seen to decrease in amplitude as time increases. This is due to the motion of the HDF (Region 2) overtaking much of the channel length, causing the magnitude of force terms plotted in Fig. 8(a) and (b) to decrease.

Fig. 8(c) provides a plot of momentum versus time, illustrating how inlet (Region 1) momentum, Region 3 liquid and vapor momentum, as well as total momentum in Region 3 change versus time. At the outset, momentum in Region 3 is equal to that in Region 1 and is primarily composed of liquid phase momentum. Liquid phase momentum is quickly reduced, however (due primarily to the influence of body force seen in Fig. 8(a)), with total momentum in Region 3 becoming equal to that of vapor momentum around the 0.1 s mark.

Fig. 8(d) illustrates how phase velocities in Region 3 change over the same period, with liquid velocity dropping to near-zero along with its momentum in Fig. 8(c), while vapor velocity decreases initially then seems to reach a steady value.

However, even though vapor velocity levels out, vapor mass velocity continues increasing with time, illustrated in Fig. 8(e). This is due to the increase in channel average quality with time, giving the vapor phase a significantly larger flow area compared to that of the liquid. Fig. 8(f) shows channel average flow quality versus time, and provides an important physical validation for the model: namely, that average flow quality in the region downstream of the HDF (Region 3) becomes near-unity just prior to the passage of the HDF out of the channel (indicating dryout has occurred downstream of the HDF). This was seen in flow visualization images analyzed in Fig. 2 as well as in multiple figures in the companion study [55], and that the model predicts this provides an important intermediate verification of the model's validity.

Fig. 8(g) illustrates the changes in phase flow areas corresponding to the continuously increasing channel average quality seen in Fig. 8(f). Two key features of this plot are (1) that the summation of phase areas is always equal to the total cross-sectional area of the channel, shown here with a solid line, and (2) even though liquid phase momentum becomes near-zero around 0.1 s (seen in Fig. 8(c)), there is still a small amount of liquid content in the downstream region which is slowly removed via phase change and very slow advection (evidenced by the very low value of liquid phase mass velocity in Fig. 8(e)).

Finally, Fig. 8(h) shows how both adiabatic and heated (diabatic) lengths change versus time. Initially the HDF is unmoving, and only once its minimum mass condition (described in the preceding section) is met does it depart. The change in adiabatic length within Region 3 versus time illustrates the initial acceleration of the HDF (evidenced by the non-linear change in l_a versus time), which eventually gives way to a more linear HDF velocity (seen in the lesser inflection in change of l_d versus time).

Similar to Fig. 8, Fig. 9 provides plots of important Region 2 (HDF) model sub-components for the same case as Fig. 8. Fig. 9 (a) begins by providing plots of relative phase velocities between the HDF (Region 2) and the upstream (Region 1) and downstream (Region 3) portions of the channel. As mentioned when discussing Fig. 5, these velocities are limited to values $\geqslant 0$.

Fig. 9(a) shows how, prior to the HDF's departure, relative velocities between the Regions 1 and 2 remain constant, while those between Regions 3 and 2 decrease due to the decreasing phase velocities within Region 3 (seen in Fig. 8(d)). After the HDF departs, relative velocities between Regions 1 and 2 also begin to decrease due to the motion of the HDF relative to the fixed velocities in the inlet region.

Fig. 9(b) indicates how mass accumulates within the HDF due to the differences in relative velocities between Regions 1 and 2 and Regions 2 and 3. Mass increases quickly at first due to differences in relative liquid phase velocities, but as these go to zero in Fig. 9(a) and only relative vapor velocities are present the rate of mass accumulation slows significantly.

Fig. 9(c) shows the evolution of force terms acting on the HDF versus time. It is clear that pressure drop and body force dominate, with the difference in momentum fluxes between Regions 1 and 2 and Regions 2 and 3 playing a significantly role immediately after the HDF departs which decreases over time (as relative velocities decrease, shown in Fig. 9(a)).

Fig. 9(d) shows the cumulative effect of these components in the form of a plot for the HDF's momentum versus time, which is used along with the mass shown in Fig. 9(b) to calculate the HDF's velocity, shown in Fig. 9(e).
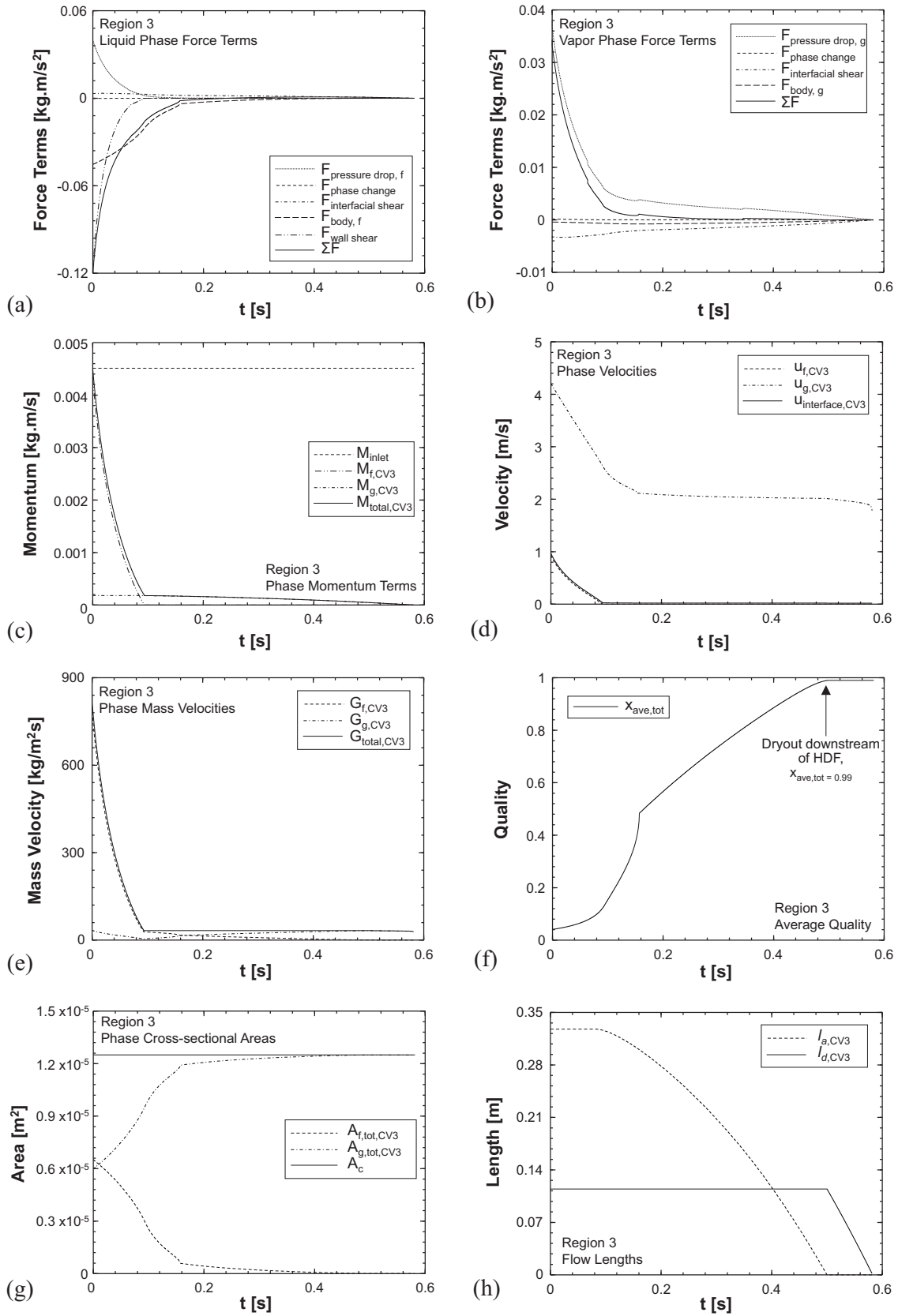
Fig. 8. Plots of Region 3 model subcomponents predictions versus time: (a) SFM force terms for liquid phase and (b) vapor phase, (c) phase momentum terms, (d) phase velocities, (e) mass velocities, (f) average quality, (g) phase cross-sectional areas, and (h) flow lengths, all for the case with mass velocity G = 835.9 kg/m²s, inlet pressure P_{in} = 122 kPa, inlet quality $x_{e,in}$ = 0.04, and FBM heat flux q'' = 2.5 W/cm².
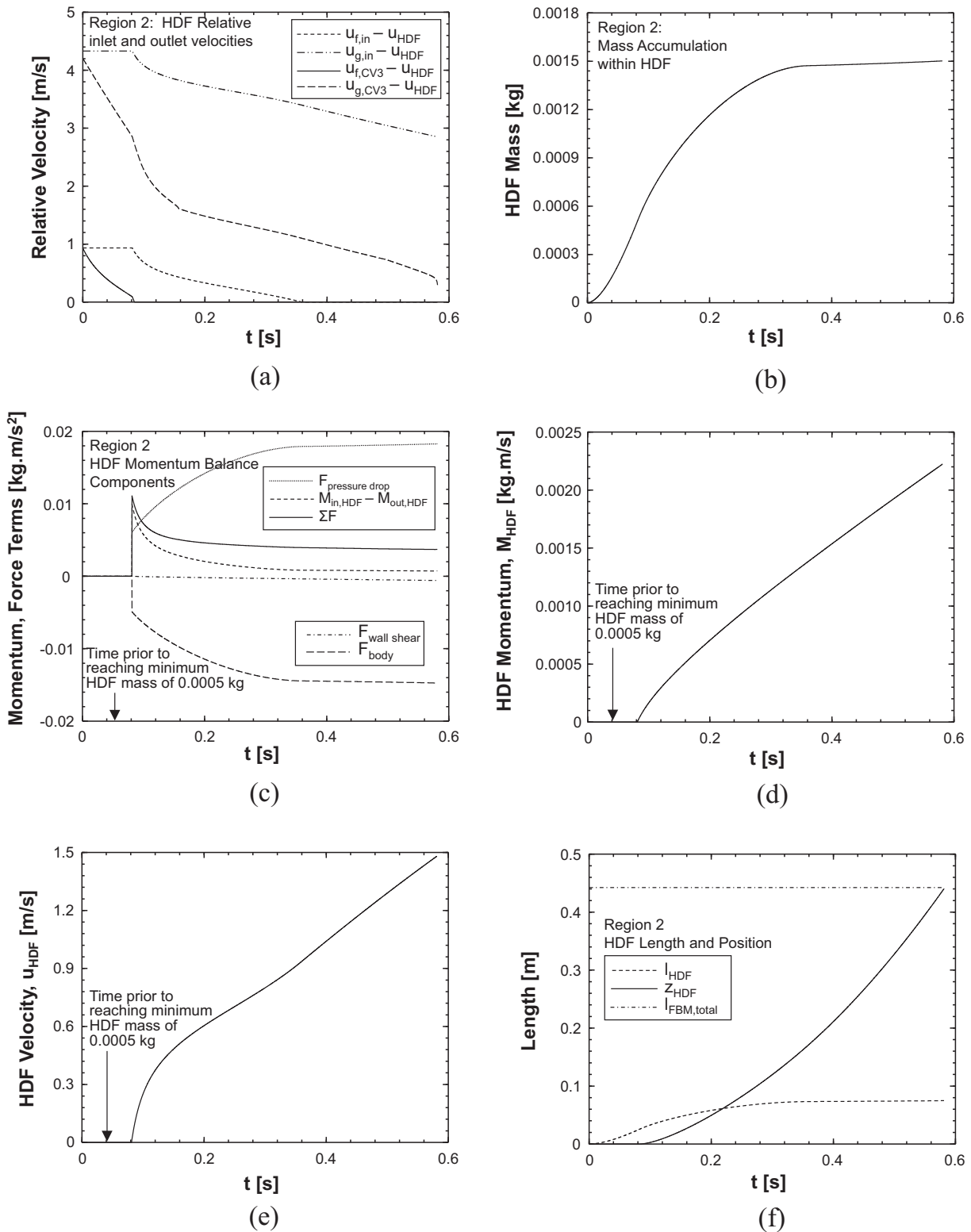
Fig. 9. Plots of Region 2 (HDF) model subcomponents predictions versus time: (a) relative velocities entering and exiting HDF, (b) mass accumulation within HDF, (c) HDF momentum balance components, (d) HDF momentum, (e) HDF velocity, and (f) HDF length and position, all for the case with mass velocity $G = 835.9$ kg/m^{2}s, inlet pressure $P_{in} = 122$ kPa, inlet quality $x_{e,in} = 0.04$, and FBM heat flux $q'' = 2.5$ W/cm^2.

Finally, Fig. 9(f) illustrates how the position of the HDF approaches the end of the channel, while the length of the HDF is simultaneously changing. It is clear that, for the current case, the maximum length of the HDF is ~0.08 m, which seems to be a

physical value when comparing with the size of HDFs seen in prior flow visualization images.

To reinforce this idea, Fig. 10 provides flow visualization images covering the 0.1146 m heated length of FBM for three different sets
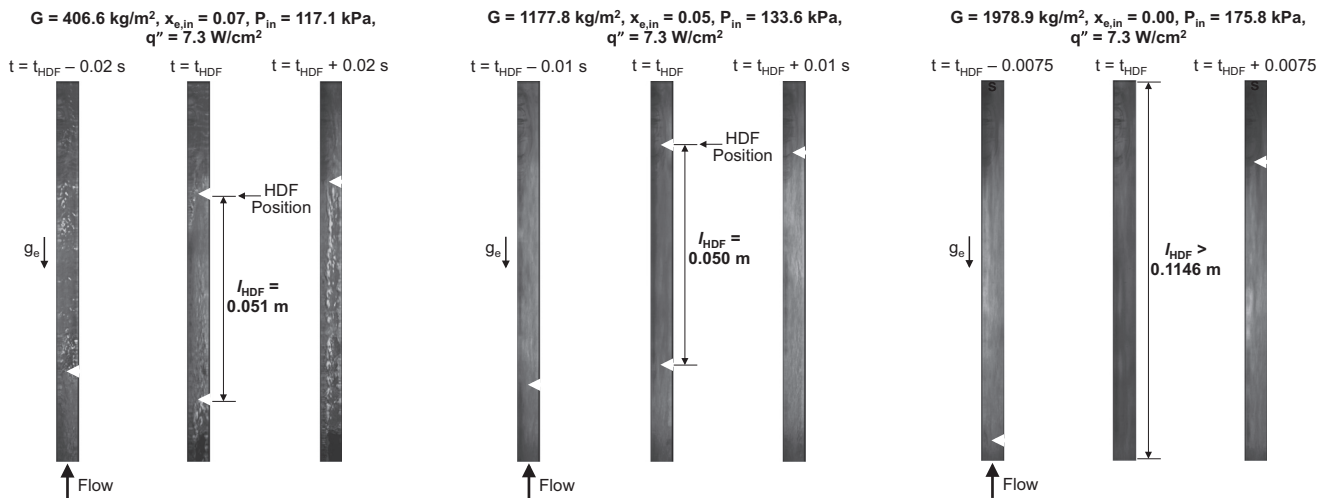
Fig. 10. Measurements of HDF length for three different sets of operating conditions.

of operating conditions, allowing for estimation of the length of the HDF in each case.

The first case in Fig. 10 shows three images for the case of $G = 406.6$ kg/m^2 s, inlet pressure $P_{in} = 117.1$ kPa, inlet quality $x_{e,in} = 0.07$, and FBM heat flux $q'' = 7.3$ W/cm^2. The first image indicates the presence of dryout in the downstream portion of the FBM heated length just prior to the arrival of the HDF (indicated with a white arrow), the second shows the body of the HDF occupying the majority of the heated length, and the third image shows a return to annular flow in the wake of the HDF (all of which serve to further validate assumptions made while modeling the behavior of Regions 1, 2, and 3).

As the height of the FBM is known to be 5 mm, it was possible to import the image into the 2-D drafting software Draftsight, use channel height as a reference dimension, and determine the length of the HDF. It should be noted that the exact beginning and end of the HDF are not clearly defined in images, so the lengths measured using this technique should not be considered as exact.

The second and third cases in Fig. 10 provide similar plots for cases of $G = 1177.8$ kg/m^2 s, inlet pressure $P_{in} = 133.6$ kPa, inlet quality $x_{e,in} = 0.05$, and FBM heat flux $q'' = 7.3$ W/cm^2, and $G = 1978.9$ kg/m^2 s, inlet pressure $P_{in} = 175.8$ kPa, inlet quality $x_{e,in} = 0.00$, and FBM heat flux $q'' = 7.3$ W/cm^2, respectively. Two features of these subfigures are of significance to the ongoing analysis. First, the HDFs identified no longer appear to be composed of continuous liquid phase as in the first case, but rather liquid distributed within vapor to the point it is unclear which should be considered the continuous phase. The second feature is the significant length of the HDF in the third case, indicating it is longer than the entire 0.1146-m heated length of FBM.

It is important to recall the definition of l_{HDF} in the model as being mass of the HDF divided by the density of liquid times the cross-sectional area of the channel, thus implying the assumption that the HDF is composed entirely of liquid. Flow visualization images reveal that this is not the case, especially at higher velocities, where it appears up to ∼50% of the HDF (by volume) can be composed of vapor phase. Thus, although the length of the HDF may increase, it is likely the mass stored within the HDF decreases as mass velocity is increased, matching the trend predicted by the model as discussed later.

Having fully outlined model construction, provided all relevant model relations and solution technique, as well as investigated sub-component trends to provide important intermediate validation of model physics, it is now possible to discuss model results

for prediction of frequency and amplitude of DWO induced pressure oscillations.

5. DWO model evaluation

Prior to comparing model predictions with associated experimental results, it was necessary to first determine exact experimental values for frequency and amplitude of DWO induced pressure oscillations. This was a major focus of the companion work to the present study [55], and will not be replicated in full herein. Appendix A provides an overview of the technique used for determining experimental values of frequency and amplitude, but for full details the original work should be consulted.

5.1. Parametric trends of model predictions

Prior to evaluating the entire 236 point database to determine overall performance statistics for the model, response to changes in key operating conditions (such as mass velocity, inlet quality, and heat flux) were first assessed to determine physical validity of model parametric trends. Experimental results shown here were all gathered in Year 1.

Fig. 11 provides plots of both amplitude and frequency versus changes in mass velocity (Fig. 11(a) and (b)), inlet quality (Fig. 11 (c) and (d)), and heat flux (Fig. 11(e) and (f)). Model simulations run to create these plots involved holding all inputs other than the parameter of interest constant. Experimental data points were selected which mirrored the model conditions as closely as possible, although it was not possible to hold all experimental parameters other than the one of interest exactly constant.

Fig. 11(a) indicates the model predicts a linear increase in frequency of oscillation as mass velocity increases, a trend that is largely mirrored by the experimental data points. A slight difference in trend is present for three highest mass velocity data points, deviating slightly from the linear relationship seen prior to that point, but this is likely attributable to the significant increase in operating pressure for these points, along with changes in inlet quality (which will be seen to have an impact on frequency of oscillation in Fig. 11(c)).

Fig. 11(b) illustrates the model is able to very accurately capture the trend of exponentially increasing amplitude of DWO induced pressure oscillations as mass velocity is increased. Experimental and analytic values exhibit a nearly exact match in trend, indicat-

ing the dependence of amplitude on mass velocity is being captured adequately by the current model.

Fig. 11(c) demonstrates how values of frequency change for changes in inlet quality to the test section (quality in Region 1 of the model). As inlet quality initially increases from a near-zero value frequency of oscillation also increases, until a peak value is reached near the $x_{e,in} = 0.45$ point, past which frequency is seen

to decrease. This trend can be explained in terms of Region 1 phase velocities: for a constant mass flow rate in Region 1, as inlet quality is increased from zero both vapor and liquid phase velocities are increased to provide the same mass flow rate. This causes larger momentum flux differences across the HDF as dryout begins to occur in Region 3, leading to higher acceleration values for the HDF. However, as quality continues to increase, decreasing liquid
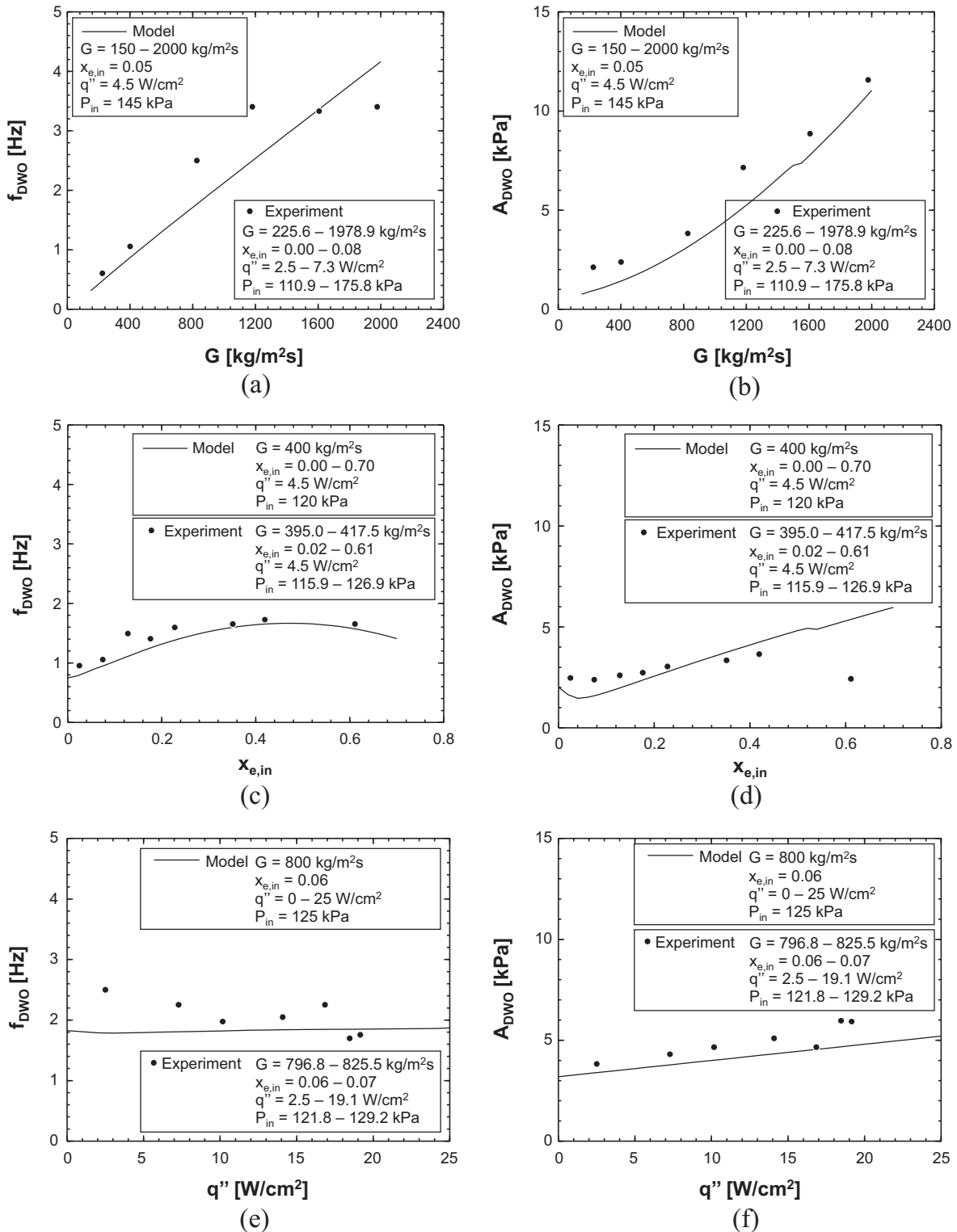

Fig. 11. Comparison of parametric trends for model predictions and experimental results: (a) DWO frequency versus mass velocity, (b) DWO amplitude versus mass velocity, (c) frequency versus inlet quality, (d) amplitude versus inlet quality, (e) frequency versus heat flux, and (f) amplitude versus heat flux.

content within the channel causes formation of the HDF to take longer, thus decreasing the frequency of oscillation despite increased HDF velocity.

Fig. 11(d) demonstrates a slight decline in amplitude of induced pressure fluctuations as inlet quality is increased prior to a near-linear increase. The experimental data mirrors this closely, with the exception of the final point, which shows significant deviation from the trend. Similar to the discussion accompanying Fig. 11(a), this is likely attributable to changes in pressure and/or mass velocity present in the experimental data not recreated in the model predictions.

Fig. 11(e) presents trends for frequency of oscillation versus heat flux applied to the heated length of FBM. The model predicts a neutral relationship between frequency and heat flux, which is largely identical to that of experimental results. Experimental results do indicate some fluctuations in frequency values, but again, these are likely attributable to small changes in other operating conditions indicated by the insets.

Finally, Fig. 11(f) provides results for amplitude versus heat flux indicating a linear increase in amplitude of oscillation is expected for increases in heat flux. The experimental data matches well with the predicted values, indicating the effect of heat flux is well captured by the model.

Overall, Fig. 11 verifies that model trends for changes in mass velocity, inlet quality, and heat flux are physical in nature and match well with experimental results. This serves to further signify the model is capable of capturing the key physical processes governing the manifestation of DWOs in vertical upflow with finite inlet quality.

5.2. Model evaluation using experimental database

As discussed in Section 2, a database of 236 operating conditions for which DWO induced behavior was observed in vertical upflow was constructed, spanning two separate years of testing. Experimental trends encountered while analyzing this database were discussed extensively in the companion study [55], and in the present study operating conditions for all 236 points were used to generate model predictions for frequency and amplitude of DWO induced pressure oscillations which were then compared with experimentally measured values to determine the overall predictive capabilities of the model.

Fig. 12 provides plots of predicted frequency versus experimental frequency of DWO induced pressure oscillations for identical sets of operating conditions. The database was subdivided into low and high mass velocity cases (Fig. 12(a) and (b)), low and high inlet quality cases (Fig. 12(c) and (d)), and low and high heat flux cases (Fig. 12(e) and (f)) to determine how the model handles different ranges of operating conditions. Additionally, Fig. 12(g) provides overall results for the entire range of operating conditions present in the database.

Key statistics presented in these plots are Mean Absolute Error (MAE), defined as

$$MAE = \frac{1}{N} \sum \frac{|f_{DWO,pred} - f_{DWO,exp}|}{f_{DWO,exp}} \times 100\%, \tag{10}$$

where N is the total number of samples, and $f_{DWO,pred}$ and $f_{DWO,exp}$ refer to model-predicted and experimental values of frequency, respectively. Additionally, parameters θ and ζ refer to the number of predictions falling within 30% and 50% of the experimental value, respectively.

Fig. 12(a) and (b) illustrates the model's ability to accurately predict frequency of oscillation for both low and high mass velocity cases, although with slightly (~7.9%) higher accuracy for high flow rate cases. In general, the highest variability in prediction accuracy

is seen for low frequency predictions (corresponding primarily to the lowest flow rate cases). As discussed in the companion study [55], experimental detection of peak frequency of oscillation is most difficult for low mass velocity cases due to lower amplitude peaks on frequency versus amplitude plots (leading to a higher 'signal-to-noise' ratio, meaning DWO induced oscillations are harder to isolate from other fluctuations), meaning some error associated with prediction of frequency for low mass velocity cases may be attributable more to measurement limitations in those cases rather than model validity.

Fig. 12(c) and (d) provides similar plots for low and high inlet quality cases, respectively. Results indicate slightly (~9.6%) better predictive accuracy is possible for lower values of flow quality, but it is worth noting that high quality cases were only possible for low mass velocities due to operating pressure limitations [53,54], meaning the degradation in predictive accuracy for high qualities cannot be solely attributed to the model's ability to account for changes in inlet quality.

Fig. 12(e) and (f) provides plots for low and high heat fluxes, respectively, which indicate little change in predictive accuracy for changes in heat flux.

Overall, Fig. 12(g) demonstrates that, for a wide range of operating conditions including tests conducted using two separate experimental facilities (although maintaining the same test module), an overall MAE of 25.5% was achieved when comparing model predictions to experimental results. Further, values of $\theta = 71.6\%$ and $\zeta = 85.2\%$ indicate the model does an excellent job of capturing overall trends for the entire range of operating conditions present in the current dataset.

Similarly, Fig. 13 provides plots of predicted versus experimental amplitude of DWO induced pressure oscillations. Values of MAE are also presented (calculated by substituting amplitudes for frequencies in Eq. (10)), along with values of θ and ζ.

Fig. 13(a) and (b) shows results for amplitude prediction corresponding to low and high mass velocities, respectively, which indicate the model offers significantly more accurate predictions for higher mass velocities. The primary source of inaccuracy for these two subfigures is found for low mass velocities, where the model significantly underpredicts amplitude of DWO induced pressure oscillations. This is likely due to the influence of virtual mass force and other effects not captured by the model which play a more significant role on HDF motion at lower mass velocities. These limitations will be discussed further in a subsequent section.

Fig. 13(c) and (d) demonstrates nearly identical predictive accuracy is achieved for both high and low ranges of inlet qualities. Similarly, Fig. 13(e) and (f) illustrates near-identical MAE values for both low and high ranges of heat flux.

Overall, Fig. 13(g) illustrates the model provides an overall MAE of 31.7% on predictions of amplitude of DWO induced pressure oscillations for the current database. Additionally, similar to the conclusion drawn when analyzing Fig. 12(g), $\theta = 50.8\%$ and $\zeta = 83.9\%$ indicate the model does an excellent job of matching general experimental trends present within the database.

5.3. Parametric extensions using model predictions

Having validated that the model provides good predictive accuracy and is capable of capturing key physical trends within the experimental dataset used for validation, an interesting continuation for analysis of the DWO phenomenon is to analyze parametric trends for changes in key operating conditions for which experimental data is not available.

Towards this end, Fig. 14 provides plots containing predictions of frequency and amplitude of DWO induced pressure oscillations for changes in local acceleration (Fig. 14(a) and (b) for frequency and amplitude, respectively), heated length (Fig. 14(c) and (d)),
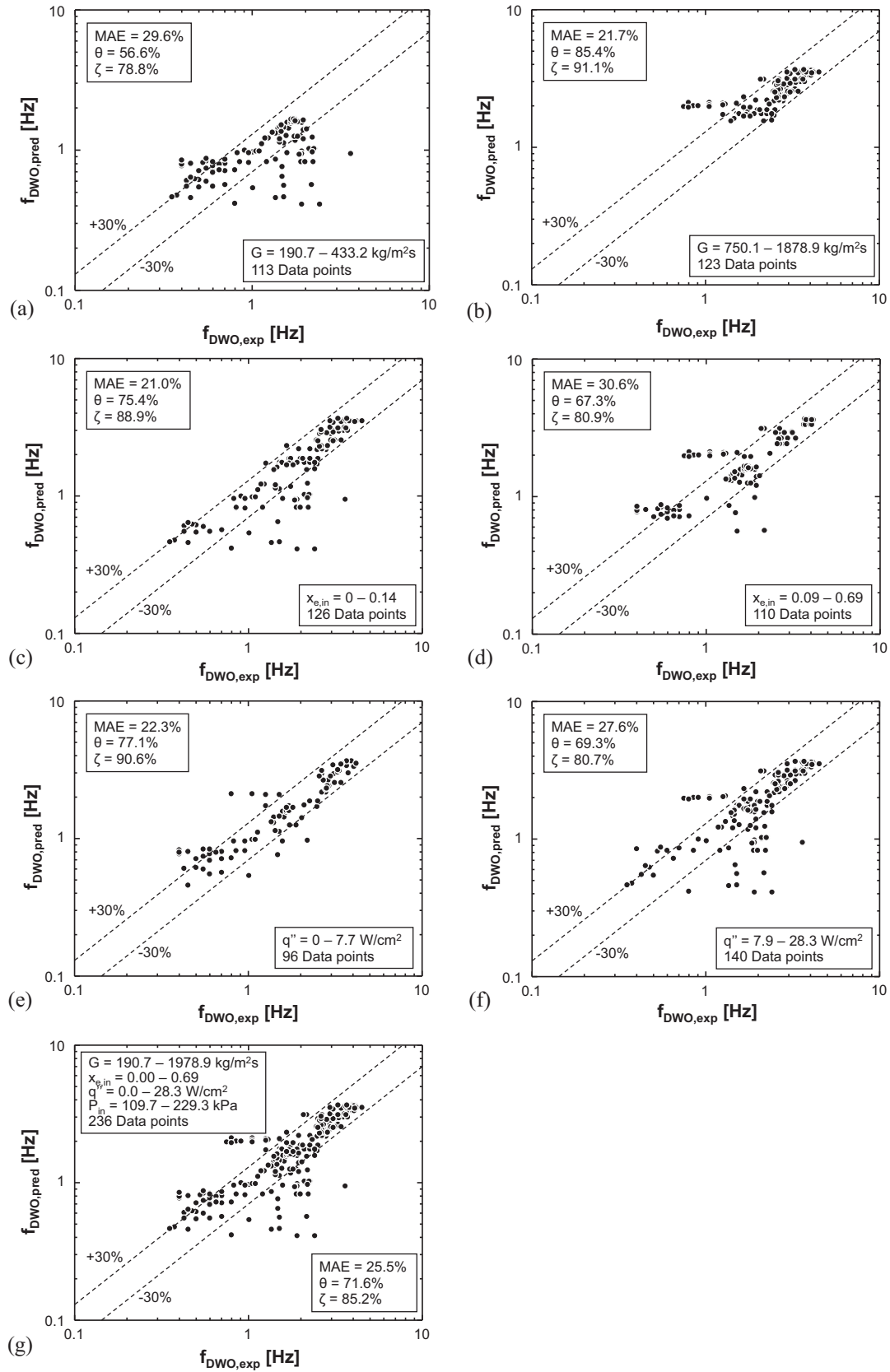
Fig. 12. Plots of DWO frequency predicted by the model versus experimentally determined values for (a) low mass flux, (b) high mass flux, (c) low inlet quality, (d) high inlet quality, (e) low heat flux, (f) high heat flux, and (g) overall range of parameters.
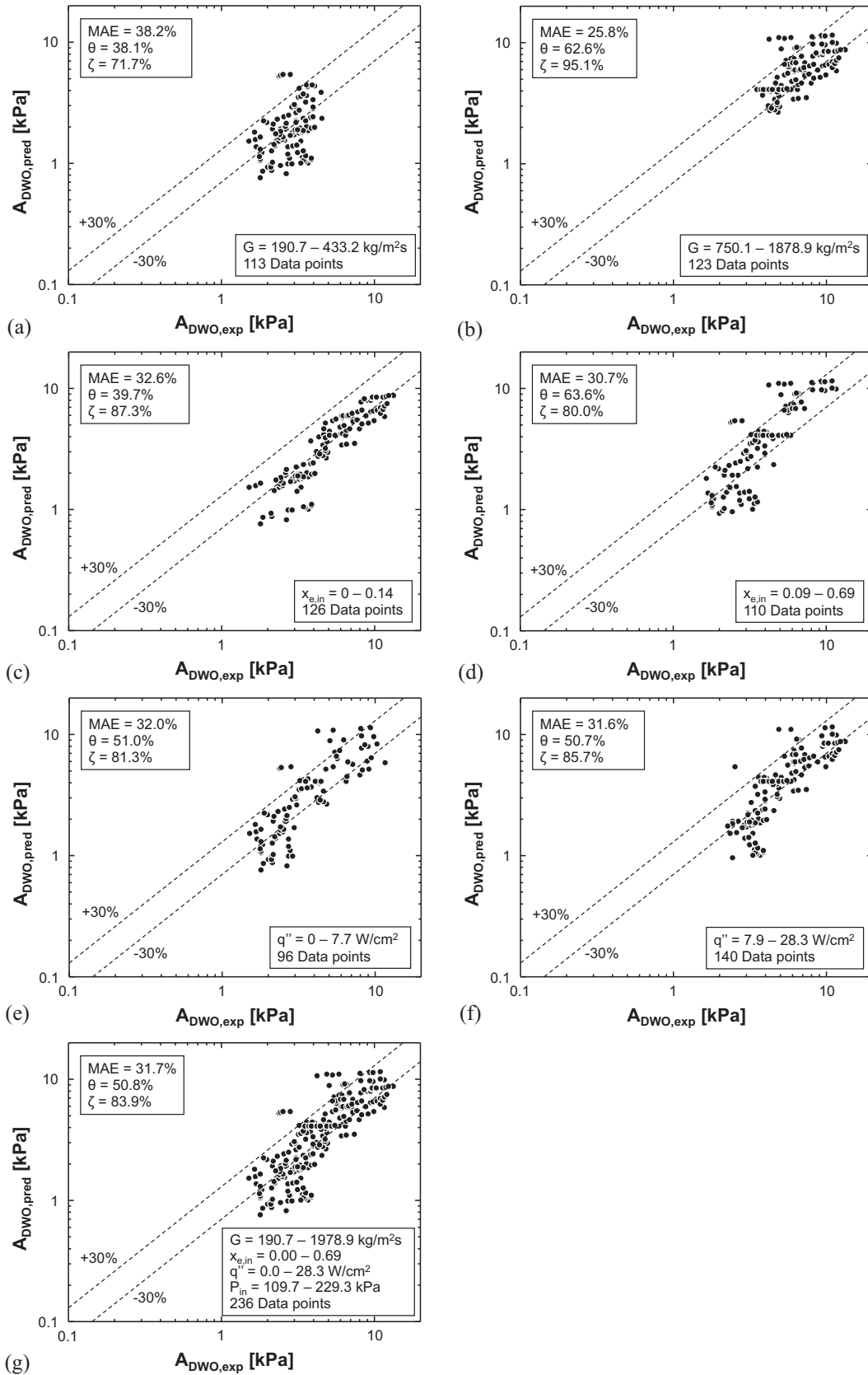
Fig. 13. Plots of DWO amplitude predicted by the model versus experimentally determined values for (a) low mass flux, (b) high mass flux, (c) low inlet quality, (d) high inlet quality, (e) low heat flux, (f) high heat flux, and (g) overall range of parameters.
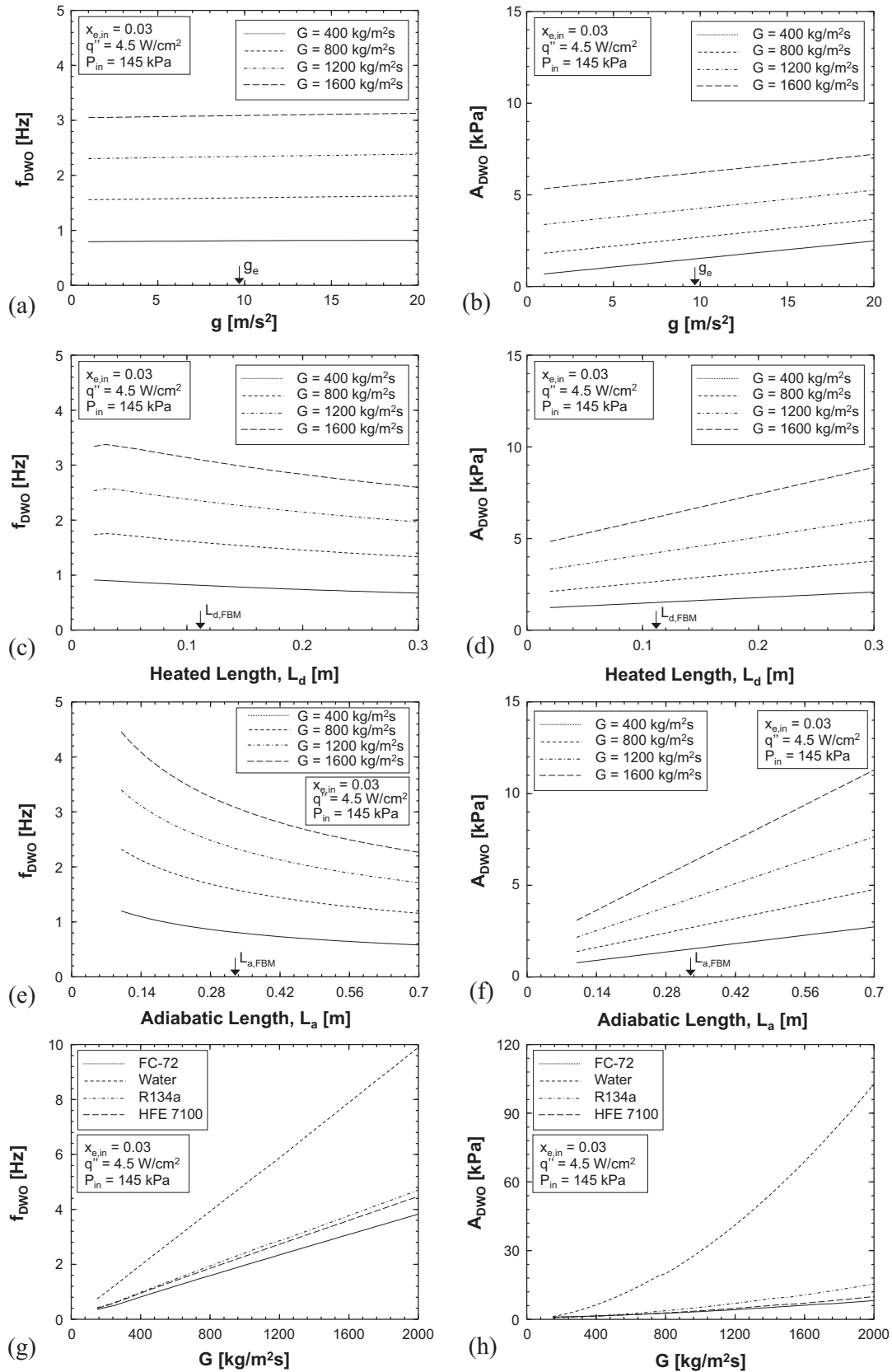
Fig. 14. Plots presenting model predictions for parametric changes to operating environment and test section geometry: (a) DWO frequency versus local acceleration (gravity), (b) DWO amplitude versus local acceleration, (c) frequency versus heated length, (d) amplitude versus heated length, (e) frequency versus adiabatic length, (f) amplitude versus adiabatic length, (g) frequency versus mass velocity for different working fluids, and (h) amplitude versus mass velocity for different working fluids.

adiabatic length (Fig. 14(e) and (f)), and working fluid (Fig. 14(g) and (h)).

Starting with Fig. 14(a), values of frequency of oscillation are seen to only vary slightly for changes in local acceleration. This is an interesting outcome, as the mechanistic description of the DWO process used to develop the model depends heavily on the role of body force, but is not necessarily invalid. It may be that only the orders of magnitude *difference* in body forces acting on liquid and vapor phases is required to incite the present instability mode, and that the magnitude of body force itself plays a minor role in determining the frequency at which the oscillations occur. It is still believed, however, that in the total absence of local acceleration this instability mode would not manifest – upcoming testing of the Flow Boiling and Condensation Experiment (FBCE) on the International Space Station (ISS) provides an excellent opportunity to test this hypothesis.

Amplitude of oscillation, however, shows significant dependence on body force, with higher values of local acceleration leading to much larger amplitudes of DWO induced pressure oscillations. This represents an important conclusion for potential applications of two-phase flow thermal management systems in applications experiencing hyper-gravity, where avoidance and/or mitigation of this instability mode may become important.

Fig. 14(c) and (d) shows predictions of frequency and amplitude of oscillation for changes in heated length of the test section indicating that frequency decreases and amplitude increases as diabatic length increases. This makes intuitive sense, as increases channel length leads to longer travel time for HDFs (leading to lower frequencies), while the same leads to increased two-phase flow pressure drop.

Similarly, Fig. 14(e) and (f) shows plots of frequency and amplitude of DWO induced pressure oscillations for changes in adiabatic length of the channel. Trends identical to those seen when analyzing Fig. 14(c) and (d) are present, although slopes of respective trendlines are slightly different due to the constant heat input in Fig. 14(e) and (f).

Finally, Fig. 14(g) and (h) provides predictions for frequency and amplitude of oscillation (respectively) versus mass velocity for four different working fluids. Immediately apparent in each subfigure is the similarity between results for FC-72, R134a, and HFE 7100, and the distinct differences for results generated using water as the working fluid.

Model predictions using water as the working fluid indicate both frequency and amplitude of DWO induced pressure oscillations will be several times larger than those using the other three working fluids. In particular, the extremely high amplitude of pressure oscillations associated with water flow at high mass velocities has the potential to significantly impact system safety considerations. It is likely that the high latent heat and surface tension of water as compared to other fluids evaluated here are responsible for these differences.

Across all subfigures in Fig. 14, it should be noted that predictions do not account for other factors present when designing and conducting flow boiling tests (*e.g.*, the presence of dryout and/or CHF for large heated lengths, onset of choked flow for high mass velocity flow of water through the present test section, *etc.*), and are simply intended to help inform future tests. Based on results shown here, conduction of tests with similar operating conditions using FC-72 in microgravity as well as Earth-based tests using water as the working fluid are of particular interest.

5.4. Discussion of model limitations and focus for future work

The model developed in the current study has been shown to be a powerful tool for predicting frequency and amplitude of DWO induced pressure oscillations, capable of accurately capturing physical trends across a wide range of operating conditions and offering high predictive accuracy. Despite this, there is room for improvement which could alleviate some shortcomings in its current formulation, primarily in the formulation of conservation of momentum for the HDF (Region 2).

As discussed alongside Fig. 5(b), conservation of momentum for Region 2 (HDF) includes the difference in momentum flux across the control-volume, pressure drop across the control-volume, viscous shear stress, and body force components. One key effect is missing, however, which is the influence of virtual mass force. Virtual mass force governs momentum interactions associated with the passage of the HDF re-wetting liquid film along the channel's walls, something that is neglected in the present model.

Similarly, boiling taking place within the HDF as it passes through the heated length of the channel is neglected, although it is possible it might play a role in creating differences in frequency and amplitude of oscillations sometimes observed between heated length inlet and outlet [55].

The final major limitation in the current model deals with the shape of the HDF itself. As the model is currently formulated, the HDF is treated as a slug of liquid advancing along the channel at a constant velocity. In reality, however, it is likely the HDF has a much higher velocity near the channel centerline, a near-zero velocity near the wall, and possibly a slight negative velocity near the wall at the trailing edge where surface tension forces are pulling liquid away to re-establish the liquid film along the wall. These effects lead the HDF to become elongated as it traverses the channel, even as it loses mass in the process (due to re-wetting of the liquid film), leading to the trend seen in Fig. 10 of increasing length and decreasing liquid composition of HDFs as mass velocity increases.

In order to better inform modeling of these phenomena, future experiments should include time-syncing of flow visualization results and transient pressure measurements to allow for instantaneous comparison of numeric and imaging results. Additionally, images captured spanning the entire length of FBM (adiabatic and diabatic lengths) could help validate modeling of mechanisms governing formation and propagation of HDFs through the channel. Finally, use of sophisticated measurement techniques such as particle image velocimetry (PIV) and laser Doppler velocimetry (LDV) to gather liquid velocity measurements both in and directly behind the HDF would allow for detailed validation of any future models seeking to develop detailed wall-normal velocity profiles within the HDF and include virtual mass force effects.

6. Conclusions

This study presented a new mechanistic model for Density Wave Oscillations for vertical upflow boiling with finite inlet quality capable of predicting frequency and amplitude of DWO induced pressure oscillations. Experimental data were analyzed and used as the basis to formulate a mechanistic description of the process by which DWOs occur within the present setup. Counter to many prior investigations which refer to DWOs as forming due to feedback effects between flow rate, pressure drop, and flow enthalpy changes causing the location of the bulk boiling boundary to fluctuate, DWOs as observed in the present work were determined to occur due to the presence of separated flow allowing for the accumulation of liquid in the channel inlet. This liquid accumulation forms a High Density Front (HDF) that departs and travels along the channel, re-wetting the liquid film and re-establishing annular, co-current flow throughout.

This cyclical process of HDF formation and passage through the channel was modeled by subdividing the channel into three key control volumes and evaluating conservation equations for each.

Model subcomponents were investigated and showed the model to exhibit physically valid trends, as did parametric evaluation of frequency and amplitude predictions. Model predictions were validated using database of 236 points where DWOs were observed experimentally and results showed the model possessing good predictive capabilities, evidenced by a Mean Absolute Error (MAE) of 25.5% when predicting frequency and 31.7% when predicting amplitude. Key findings from this study are as follows:

(1) Analysis of experimental results revealed that dominant low-frequency pressure oscillations observed in a majority of vertical upflow cases with finite inlet quality are associated with the cyclical passage of High Density Fronts (HDFs) through the test section.
(2) A physical explanation for mechanisms leading to the formation and passage of HDFs through the test section was presented, centering on the orders of magnitude difference in body forces acting on liquid and vapor phases while in a separated flow regime.
(3) A mechanistic model for DWOs was developed by analyzing the process behind formation and motion of HDFs through the test section. The model is capable of predicting frequency and amplitude of DWO induced pressure oscillations, and was shown to accurately capture physical trends for a wide parametric range. Predictive accuracy of the model was evaluated using a 236-point dataset and shown to be satisfactory.
(4) The model was used to investigate potential parametric variations not possible with current experimental facilities, and led to two key features of interest for future studies: whether this phenomenon will manifest in the absence of gravity, and that use of water as a working fluid could potentially yield pressure fluctuations of significantly higher amplitude.
(5) Limitations of the current modeling work were discussed, with the key takeaway being the need for more detailed treatment of HDF hydrodynamics.

Conflict of interest

The authors declared that there is no conflict of interest.

Acknowledgements

Appendix A. Determination of experimental amplitude and frequency of DWO induced pressure oscillations

In order to validate model predictions against experimentally observed values for frequency and amplitude of DWO induced pressure oscillations, it is first necessary to describe how these values are detected.

Fig. A1(a) shows transient pressure curves corresponding to operating conditions of G = 834.1 kg/m^2 s, $x_{e,in}$ = 0.04, P_{in} = 122.6 kPa, and q'' = 7.3 W/cm^2. Fast Fourier Transforms are performed on these transient pressure signals, with the results shown in Fig. A1(b). Peak frequency of oscillation can be found for both inlet and outlet pressure signals by searching for the frequency associated with peak amplitude of oscillation, with the search limited to frequencies in the relevant range ($\sim$0.1–10 Hz) to eliminate the false detection of frequencies associated with non-DWO induced behavior.

For this set of operating conditions, Fig. A1(b) shows both inlet and outlet pressures oscillate with peak frequency of 2.1 Hz, associated with a peak amplitude of $\sim$0.9 kPa on the amplitude versus frequency plots. Transient curves in Fig. A1(a) indicate pressures oscillate with much higher amplitudes, however, closer to $\sim$10 kPa. This difference is attributed to two effects. First, DWOs do not occur at a constant frequency, but over a narrow range of frequencies. Second, and more importantly, DWOs are not perfectly sinusoidal in behavior, and are best described using a Fourier series, or a linear combination of sine and cosine functions rather than a single function. The peak frequency detected in Fig. A1(b) is simply the frequency most closely associated (containing the most energy) with DWO induced oscillations.

Thus, alternate methodology must be employed to determine the amplitude at which DWO induced pressure fluctuations occur for a given set of operating conditions. Towards this, fluctuating pressure P' is isolated, where

$$P' = P - P_{ave}, \tag{A1}$$

with P and P_{ave} corresponding to total and time-averaged pressures, respectively. Fig. A1(c) shows plots of inlet and outlet fluctuating pressure versus time, plotted over a short period of 2 s to highlight their structure. Both curves are composed of low-frequency fluctuations with high-frequency oscillations superimposed. This conclusion can also be drawn from analyzing amplitude versus frequency plots in Fig. A1(b), which show the majority of fluctuations occur in the 1–5 Hz range, with a few sharp peaks located in the 10–100 Hz range, likely attributable to mechanically induced oscillations [54]. To remove these high-frequency fluctuations and isolate the low frequency behavior attributable to DWOs, a second-order digital Butterworth low-pass filter with a cutoff frequency of 10 Hz is used, with filter transfer function given by

$$H(z) = \frac{0.02 + 0.04z^{-1} + 0.02z^{-2}}{1.0 - 1.56z^{-1} + 0.64z^{-2}}. \tag{A2}$$

Numerator and denominator coefficients are truncated here for presentation, but are output with additional significant figures by the python function used to generate them.

Filtered pressure fluctuations are identified with dashed lines in Fig. A1(c), and clearly illustrate only low frequency fluctuations remain after applying the filter function. Analysis also reveals there is a slight phase shift between the raw and filtered signals which is characteristic of the filter type used here and does not affect the amplitude of the filtered signal.

Using the filtered pressure fluctuation curves, Fig. A1(d) illustrates how amplitude of oscillation can be determined by simply halving the difference between maximum and minimum values.

Both experimental amplitude and frequency values reported in Figs. 11–14 are determined by first detecting frequency and amplitude of pressure oscillations for both inlet and outlet (of the FBM's heated length) pressures. Then, inlet and outlet values are averaged, giving a single value for each parameter for each unique set of operating conditions.

A full discussion of the merits and limitations of this technique may be found in the companion study to the present work [55], along with comments on the validity of using a single frequency and amplitude value to re-create DWO induced oscillatory behavior.
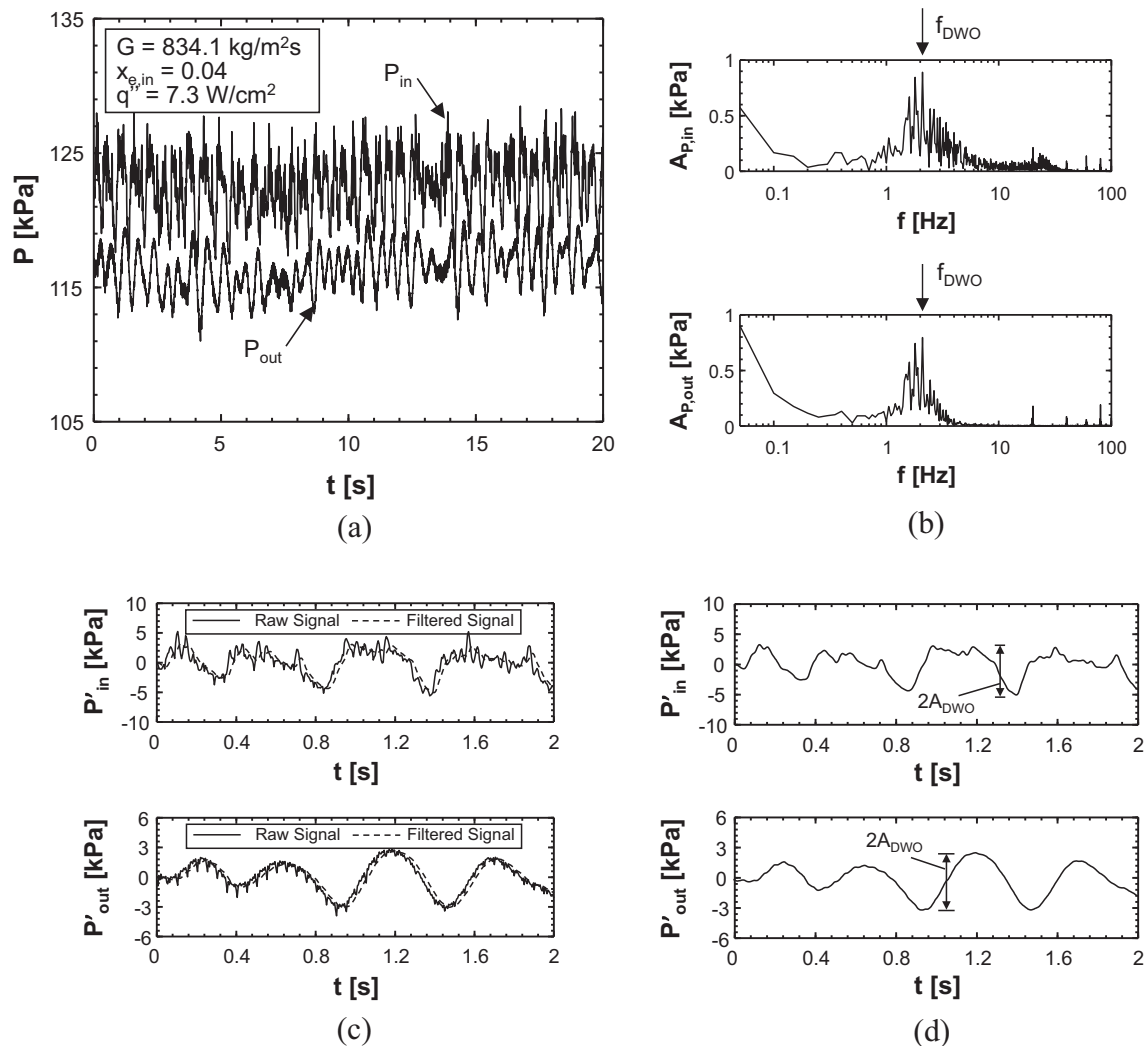
Fig. A1. Plots showing detection methodology for DWO frequency and amplitude: (a) transient inlet and outlet pressure signals for entire fast Fourier transform (FFT) window, (b) associated FFTs with peak frequencies identified, (c) low-pass filtered pressure signals to isolate DWO behavior, and (d) DWO amplitude detection using filtered signals. Adapted from [55].

Appendix B. Supplementary material

Supplementary data associated with this article can be found, in the online version, at https://doi.org/10.1016/j.ijheatmasstransfer. 2018.02.078.

References

[1] I. Mudawar, Assessment of high-heat-flux thermal management schemes, IEEE Trans. – CPMT 24 (2001) 122–141.

[2] C.L. Tien, K.S. Chung, Entrainment limits in heat pipes, AIAA J. 17 (1979) 643–646.

[3] T.J. LaClair, I. Mudawar, Thermal transients in a capillary evaporator prior to the initiation of boiling, Int. J. Heat Mass Transfer 43 (2000) 3937–3952.

[4] M. Shafahi, V. Bianco, H. Vafai, O. Manco, An investigation of the thermal performance of cylindrical heat pipes using nanofluids, Int. J. Heat Mass Transfer 53 (2010) 376–383.

[5] P.J. Marto, V.J. Lepere, Pool boiling heat transfer from enhanced surfaces to dielectric fluids, J. Heat Transfer 104 (1982) 292–299.

[6] I. Mudawar, T.M. Anderson, Parametric investigation into the effects of pressure, subcooling, surface augmentation and choice of coolant on pool boiling in the design of cooling systems for high-power density chips, J. Electron. Packag. 112 (1990) 375–382.

[7] S.J. Reed, I. Mudawar, Elimination of boiling incipience temperature drop in highly wetting fluids using spherical contact with a flat surface, Int. J. Heat Mass Transfer 42 (1999) 2439–2454.

[8] J.A. Shmerler, I. Mudawar, Local heat transfer coefficient in wavy free-falling turbulent liquid films undergoing uniform sensible heating, Int. J. Heat Mass Transfer 31 (1988) 67–77.

[9] I. Mudawar, R.A. Houpt, Mass and momentum transport in smooth falling liquid films laminarized at relatively high Reynolds numbers, Int. J. Heat Mass Transfer 36 (1993) 3437–3448.

[10] C.O. Gersey, I. Mudawar, Effects of heater length and orientation on the trigger mechanism for near-saturated flow boiling CHF – I. Photographic and statistical characterization of the near-wall interfacial features, Int. J. Heat Mass Transfer 38 (1995) 629–642.

[11] S.M. Ghiaasiaan, Two-phase Flow, Boiling and Condensation in Conventional and Miniature Systems, Cambridge University Press, New York, 2008.

[12] W. Qu, I. Mudawar, Thermal design methodology for high-heat-flux single-phase and two-phase micro-channel heat sinks, in: Proc. I-THERM 2002, San Diego, California, 2002, pp. 347–359.

[13] S. Mukherjee, I. Mudawar, Smart pumpless loop for micro-channel electronic cooling using flat and enhanced surfaces, IEEE Trans. – CPMT 26 (2003) 99–109.

[14] S. Mukherjee, I. Mudawar, Pumpless loop for narrow channel and micro-channel boiling from vertical surfaces, J. Electron. Packag. 125 (2003) 431–441.

[15] J. Lee, I. Mudawar, Critical heat flux for subcooled flow boiling in micro-channel heat sinks, Int. J. Heat Mass Transfer 52 (2009) 3341–3352.

[16] J. Lee, I. Mudawar, Fluid flow and heat transfer characteristics of low temperature two-phase micro-channel heat sinks – part 1: experimental methods and flow visualization results, Int. J. Heat Mass Transfer 51 (2008) 4315–4326.

[17] M. Monde, T. Inoue, Critical heat flux in saturated forced convective boiling on a heated disk with multiple impinging jets, J. Heat Transfer 113 (1991) 722–727.

[18] D.C. Wadsworth, I. Mudawar, Enhancement of single-phase heat transfer and critical heat flux from an ultra-high-flux simulated microelectronic heat source to a rectangular impinging jet of dielectric liquid, J. Heat Transfer 114 (1992) 764–768.

[19] M.E. Johns, I. Mudawar, An ultra-high power two-phase jet-impingement avionic clamshell module, J. Electron. Packag. 118 (1996) 264–270.

[20] I. Mudawar, Recent advances in high-flux, two-phase thermal management, J. Therm. Sci. Eng. Appl. 5 (2013) 021012.

[21] W.P. Klinzing, J.C. Rozzi, I. Mudawar, Film and transition boiling correlations for quenching of hot surfaces with water sprays, J. Heat Treating 9 (1992) 91–103.

[22] D.D. Hall, I. Mudawar, Optimization of quench history of aluminum parts for superior mechanical properties, Int. J. Heat Mass Transfer 39 (1996) 85–95.

[23] L. Lin, R. Ponnappan, Heat transfer characteristics of spray cooling in a closed loop, Int. J. Heat Mass Transfer 46 (2003) 3737–3746.

[24] J.D. Bernardin, I. Mudawar, A Leidenfrost point model for impinging droplets and sprays, J. Heat Transfer 126 (2004) 272–278.

[25] M. Visaria, I. Mudawar, Effects of high subcooling on two-phase spray cooling and critical heat flux, Int. J. Heat Mass Transfer 51 (2008) 5269–5278.

[26] I. Mudawar, D. Bharathan, K. Kelly, S. Narumanchi, Two-phase spray cooling of hybrid vehicle electronics, IEEE Trans. – CPMT 32 (2009) 501–512.

[27] M. Visaria, I. Mudawar, Application of two-phase spray cooling for thermal management of electronic devices, IEEE Trans. – CPMT 32 (2009) 784–793.

[28] I. Mudawar, Two-phase micro-channel heat sinks: theory, applications and limitations, J. Electron. Packag. 133 (2011) 041002–41012.

[29] M.K. Sung, I. Mudawar, Experimental and numerical investigation of single-phase heat transfer using a hybrid jet impingement/micro-channel cooling scheme, Int. J. Heat Mass Transfer 49 (2006) 682–694.

[30] M.K. Sung, I. Mudawar, Single-phase hybrid micro-channel/jet impingement cooling, Int. J. Heat Mass Transfer 51 (2008) 4342–4352.

[31] M.K. Sung, I. Mudawar, Single-phase and two-phase heat transfer characteristics of low temperature hybrid micro-channel/micro-jet impingement cooling module, Int. J. Heat Mass Transfer 51 (2008) 3882–3895.

[32] S. Lee, I. Mudawar, M.M. Hasan, Thermal analysis of hybrid single-phase, two-phase and heat pump thermal control system (TCS) for future spacecraft, Appl. Therm. Eng. 100 (2016) 190–214.

[33] F.P. Chiramonte, J.A. Joshi, Workshop on Critical Issues in Microgravity Fluids, Transport, and Reaction Processes in Advanced Human Support Technology – Final Report, NASA TM-2004-212940, 2004.

[34] The National Academies, Recapturing a Future for Space Exploration: Life and Physical Sciences Research for a New Era, National Academies Press, Washington, DC, 2011.

[35] H. Zhang, I. Mudawar, M.M. Hasan, Flow boiling CHF in microgravity, Int. J. Heat Mass Transfer 48 (2005) 3107–3118.

[36] H. Zhang, I. Mudawar, M.M. Hasan, Application of flow boiling for thermal management of electronics in microgravity and reduce-gravity space systems, IEEE Trans. – CPMT 32 (2009) 466–477.

[37] M. Ishii, N. Zuber, Thermally induced instabilities in two-phase mixtures, Proc. 4th Int. Heat Transfer Conf. on Heat Transfer, Paris, 1970, Paper B5.11.

[38] D. Brutin, L. Tadrist, Pressure drop and heat transfer analysis of flow boiling in a minichannel: influence of the inlet condition on two-phase flow stability, Int. J. Heat Mass Transfer 47 (2004) 2365–2377.

[39] G. Wang, P. Cheng, A.E. Bergles, Effects of inlet/outlet configurations on flow boiling instability in parallel microchannels, Int. J. Heat Mass Transfer 51 (2008) 2267–2281.

[40] R.H. Whittle, R. Forgan, A correlation for the minima in the pressure drop versus flow-rate curves for sub-cooled water flowing in narrow heated channels, Nucl. Eng. Des. 6 (1967) 89–99.

[41] J.E. Kennedy, G.M. Roach Jr., M.F. Dowling, S.I. Abdel-Khalik, S.M. Ghiaasiaan, S.M. Jeter, Z.H. Qureshi, The onset of flow instability in uniformly heated horizontal microchannels, J. Heat Transfer 122 (2000) 118–125.

[42] J. Wang, Y. Huang, Y. Wang, Visualized study on specific points on demand curves and flow patterns in a single-side heated narrow rectangular channel, Int. J. Heat Fluid Flow 32 (2011) 982–992.

[43] J. Lee, H. Chae, S.H. Chang, Flow instability during subcooled boiling for a downward flow at low pressure in a vertical narrow rectangular channel, Int. J. Heat Mass Transfer 67 (2013) 1170–1180.

[44] M. Ledinegg, Instability of flow during natural and forced circulation, Die Wärme 61 (1938) 891–898.

[45] P. Saha, M. Ishii, N. Zuber, An experimental investigation of the thermally induced flow oscillations in two-phase systems, J. Heat Transfer 98 (1976) 616–622.

[46] M. Ozawa, S. Nakanishi, S. Ishigai, Y. Mizuta, H. Tarui, Flow instabilities in boiling channels: Part 1, Pressure drop oscillations, Bull. JSME 22 (1979) 1113–1118.

[47] R.T. Lahey Jr., M.Z. Podowski, On the analysis of various instabilities in two-phase flow, Multiphase Sci. Tech. 4 (1989) 183–370.

[48] E.P. Serov, The operation of once-through boiler in variable regimes, Trudy, Moscow Energy Inst. 11 (1953).

[49] G. Yadigaroglu, A.E. Bergles, Fundamental and higher-mode density-wave oscillations in two-phase systems, J. Heat Transfer 94 (1972) 189–195.

[50] J.A. Boure, A.E. Bergles, L.S. Tong, Review of two-phase flow instability, Nucl. Eng. Des. 25 (1973) 165–192.

[51] D.F. Delmastro, A. Clausse, J. Converti, The influence of gravity on the stability of boiling flows, Nucl. Eng. Des. 127 (1991) 129–139.

[52] C.W. Shin, H.C. NO, Experimental study for pressure drop and flow instability of two-phase flow in the PCHE-type steam generator for SMRs, Nucl. Eng. Des. 318 (2017) 109–118.

[53] L.E. O'Neill, C.R. Kharangate, I. Mudawar, Time-averaged and transient pressure drop for flow boiling with saturated inlet conditions, Int. J. Heat Mass Transfer 103 (2016) 133–153.

[54] L.E. O'Neill, I. Mudawar, M.M. Hasan, H.K. Nahra, R. Balasubramaniam, N.R. Hall, A. Lokey, J.R. Mackey, Experimental investigation into the impact of density wave oscillations on flow boiling system dynamic behavior and stability, Int. J. Heat Mass Transfer 120 (2018) 144–166.

[55] L.E. O'Neill, I. Mudawar, M.M. Hasan, H.K. Nahra, B. Ramaswamy, J.R. Mackey, Experimental investigation of frequency and amplitude of density wave oscillations in vertical upflow boiling, Int. J. Heat Mass Transfer (2018) (submitted for publication).

[56] W. Qu, I. Mudawar, Measurement and prediction of pressure drop in two-phase micro-channel heat sinks, Int. J. Heat Mass Transfer 46 (2003) 2737–2753.

[57] K.H. Chang, C. Pan, Two-phase flow instability for boiling in a microchannel heat sink, Int. J. Heat Mass Transfer 50 (2007) 2078–2088.

[58] H. Lee, I. Park, I. Mudawar, M.M. Hasan, Micro-channel evaporator for space applications – 1. Experimental pressure drop and heat transfer results for different orientations in Earth gravity, Int. J. Heat Mass Transfer 77 (2014) 1213–1230.

[59] M. Ozawa, S. Nakanishi, S. Ishigai, Y. Mizuta, H. Tarui, Flow instabilities in boiling channels: part 1, Pressure drop oscillations, Bull. JSME 51 (1979) 1113–1118.

[60] V. Jovic, N. Afgan, L. Jovic, D. Spasojevic, An experimental study of the pressure drop oscillations in three parallel channel two phase flow, in: G.F. Hewitt (Ed.), Proc. Int. Heat Transfer Conf., Brighton, UK, 1994, pp. 193–198.

[61] S. Lee, V.S. Devahdhanush, I. Mudawar, Frequency analysis of pressure oscillations in large length-to-diameter two-phase micro-channel heat sinks, Int. J. Heat Mass Transfer 116 (2018) 273–291.

[62] H. Yuncu, An experimental and theoretical study of density wave and pressure drop oscillations, Heat Transfer Eng. 11 (1990) 45–56.

[63] W.R. Schlichting, R.T. Lahey Jr., M.Z. Podowski, An analysis of interacting instability modes, in a phase change system, Nucl. Eng. Des. 240 (2010) 3178–3201.

[64] L. Tadrist, Review on two-phase flow instabilities in narrow spaces, Int. J. Heat Fluid Flow 28 (2007) 54–62.

[65] S. Kakac, B. Bon, A review of two-phase flow dynamic instabilities in tube boiling systems, Int. J. Heat Mass Transfer 51 (2008) 399–433.

[66] L.C. Ruspini, C.P. Marcel, A. Clausse, Two-phase flow instabilities: a review, Int. J. Heat Mass Transfer 71 (2014) 521–548.

[67] J. Barber, K. Sefiane, D. Brutin, L. Tadrist, Hydrodynamics and heat transfer during flow boiling instabilities in a single microchannel, Appl. Therm. Eng. 29 (2009) 1299–1308.

[68] S. Lee, I. Mudawar, Transient characteristics of flow boiling in large micro-channel heat exchangers, Int. J. Heat Mass Transfer 103 (2016) 186–202.

[69] S. Lee, I. Mudawar, Thermal and thermodynamic performance, and pressure oscillations of refrigeration loop employing large micro-channel evaporators, Int. J. Heat Mass Transfer 103 (2016) 1313–1326.

[70] Q. Lu, D. Chen, C. Li, X. He, Experimental investigation on flow boiling heat transfer in conventional and mini vertical channels, Int. J. Heat Mass Transfer 107 (2017) 225–243.

[71] G. Xia, W. Wang, L. Cheng, D. Ma, Visualization study on the instabilities of phase-change heat transfer in a flat two-phase closed thermosyphon, App. Therm. Eng. 116 (2017) 392–405.

[72] K. Miyoshi, N. Takenaka, T. Ishida, K. Sugimoto, Investigation of temperature fluctuation phenomena in a stratified steam-water two-phase flow in a simulating pressurizer spray pipe of a pressurized water reactor, Nucl. Eng. Des. 316 (2017) 38–45.

[73] C. Huh, J. Kim, M.H. Kim, Flow pattern transition instability during flow boiling in a single microchannel, Int. J. Heat Mass Transfer 50 (2007) 1049–1060.

[74] C.A. Chen, T.F. Lin, W.-M. Yan, Time periodic saturated flow boiling heat transfer of R-134a in a narrow annular duct due to heat flux oscillation, Int. J. Heat Mass Transfer 106 (2017) 35–46.

[75] M. Ishii, Thermally Induced Flow Instabilities in Two-phase Mixtures in Thermal Equilibrium (Ph.D. Thesis), Georgia Institute of Technology, 1971.

[76] H. Nyquist, Regeneration theory, Bell Syst. Techn. J. 11 (1932) 126.

[77] S. Levy, E.S. Beckjord, Hydraulic Instability in a Natural Circulation Loop with Net Steam Generation at 1000 psia, G.E.A.P., 3215, General Electric, 1959.

[78] K. Solberg, Resulats des essaisd' instabilities sur la boucle 'culine' et comparisons avec un code de calcul, C.E.N.G., Note 225, Centre d'Etudes Nucleaires de Grenoble, France, 1966.

[79] M.B. Carver, An Analytical Model for the Prediction of Hydro-dynamic Instability in Parallel Heated Channels, A.E.C.L., 2681, Atomic Energy Canada Limited, 1968.

[80] K. Fukuda, T. Kobori, Classification of two-phase flow instability by density wave oscillation model, J. Nucl. Sci. Technol. 16 (1979) 95–108.

[81] L.A. Belblidia, C. Bratianu, Density-wave oscillations, Ann. Nucl. Energy 6 (1979) 425–444.

[82] J.-L. Achard, D.A. Drew, R.T. Lahey, The analysis of nonlinear density-wave oscillations in boiling channels, J. Fluid Mech. 155 (1985) 213–232.

[83] Q. Wang, X.J. Chen, S. Kakac, Y. Ding, An experimental investigation of density-wave-type oscillations in a convective boiling upflow system, Int. J. Heat Fluid Flow 3 (1994) 241–246.

[84] V. Pandey, S. Singh, Characterization of stability limits of Ledinegg instability and density wave oscillations for two-phase flow in natural circulation loops, Chem. Eng. Sci. 168 (2017) 204–224.

[85] I. Mudawar, Flow boiling and flow condensation in reduced gravity, Adv. Heat Transfer 49 (2017) 225–306.

[86] S.M. Kim, I. Mudawar, Universal approach to predicting saturated flow boiling heat transfer in mini/micro-channels – Part II. Two-phase heat transfer coefficient, Int. J. Heat Mass Transfer 64 (2013) 1239–1256.

[87] S.M. Kim, I. Mudawar, Theoretical model for local heat transfer coefficient for annular flow boiling in circular mini/micro-channels, Int. J. Heat Mass Transfer 73 (2014) 731–742.

[88] S.M. Kim, I. Mudawar, Condensation in parallel micro-channels – Part 2: Heat transfer results and correlation technique, Int. J. Heat Mass Transfer 55 (2012) 984–994.

[89] C.R. Kharangate, L.E. O'Neill, I. Mudawar, Effects of two-phase inlet quality, mass velocity, flow orientation, and heating perimeter on flow boiling in a rectangular channel: Part 1 – two-phase flow and heat transfer results, Int. J. Heat Mass Transfer 103 (2016) 1261–1279.

[90] S.-M. Kim, I. Mudawar, Universal approach to predicting two-phase frictional pressure drop for mini/micro-channel saturated flow boiling, Int. J. Heat Mass Transfer 55 (2013) 718–734.

[91] S.-M. Kim, J. Kim, I. Mudawar, Flow condensation in parallel micro-channels – Part 1: experimental results and assessment of pressure drop correlations, Int. J. Heat Mass Transfer 55 (2012) 971–983.

[92] H. Zhang, I. Mudawar, M.M. Hasan, Experimental assessment of the effects of body force, surface tension force, and inertia on flow boiling CHF, Int. J. Heat Mass Transfer 45 (2002) 4079–4095.

[93] H. Zhang, I. Mudawar, M.M. Hasan, Experimental and theoretical study of orientation effects on flow boiling CHF, Int. J. Heat Mass Transfer 45 (2002) 4463–4478.

[94] C. Konishi, I. Mudawar, Review of flow boiling and critical heat flux in microgravity, Int. J. Heat Mass Transfer 80 (2015) 469–493.

[95] C.R. Kharangate, L.E. O'Neill, I. Mudawar, M.M. Hasan, H.K. Nahra, R. Balasubramaniam, N.R. Hall, A.M. Macner, J.R. Mackey, Effects of subcooling and two-phase inlet on flow boiling heat transfer and critical heat flux in a horizontal channel with one-sided and double-sided heating, Int. J. Heat Mass Transfer 91 (2015) 1187–1205.

[96] C.R. Kharangate, L.E. O'Neill, I. Mudawar, M.M. Hasan, H.K. Nahra, R. Balasubramaniam, N.R. Hall, A.M. Macner, J.R. Mackey, Flow boiling and critical heat flux in horizontal channel with one-sided and double-sided heating, Int. J. Heat Mass Transfer 90 (2015) 323–338.

[97] C.R. Kharangate, C. Konishi, I. Mudawar, Consolidated methodology to predicting flow boiling critical heat flux for inclined channels in Earth gravity and for microgravity, Int. J. Heat Mass Transfer 92 (2016) 467–482.

[98] C.R. Kharangate, L.E. O'Neill, I. Mudawar, Effects of two-phase inlet quality, mass velocity, flow orientation, and heating perimeter on flow boiling in a rectangular channel: Part 2 – CHF experimental results and model, Int. J. Heat Mass Transfer 103 (2016) 1280–1296.

[99] C.F. Colebrook, Turbulent flow in pipes, with particular reference to the transition region between the smooth and rough pipe laws, J. Inst. Civ. Eng. 11 (1939) 133–156.

[100] G.B. Wallis, One-dimensional Two-phase Flow, McGraw-Hill, New York, 1969.

[101] W.W. Akers, H.A. Deans, O.K. Crosser, Condensing heat transfer within horizontal tubes, Chem. Eng. Prog. 54 (1958) 89–90.

[102] S.M. Zivi, Estimation of steady-state steam void-fraction by means of the principle of minimum entropy production, J. Heat Transfer 86 (1964) 247–252.